Analysis of Hail Production via Simulated Hailstone Trajectories in the 29 May 2012 Kingfisher, Oklahoma, Supercell

LAUREN E. POUNDS[,a,b,c] CONRAD L. ZIEGLER,[b,a,c] REBECCA D. ADAMS-SELIN,[d] AND MICHAEL I. BIGGERSTAFF[a]

[a] *School of Meteorology, University of Oklahoma, Norman, Oklahoma*
[b] *NOAA/OAR/National Severe Storms Laboratory, Norman, Oklahoma*
[c] *Cooperative Institute for Severe and High-Impact Weather Research and Operations, Norman, Oklahoma*
[d] *Verisk Atmospheric and Environmental Research, Bellevue, Nebraska*

ABSTRACT: This study uses a new, unique dataset created by combining multi-Doppler radar wind and reflectivity analysis, diabatic Lagrangian analysis (DLA) retrievals of temperature and water substance, and a complex hail trajectory model to create millions of numerically simulated hail trajectories in the Kingfisher, Oklahoma, supercell on 29 May 2012. The DLA output variables are used to obtain a realistic, 4D depiction of the storm's thermal and hydrometeor structure as required input to the detailed hail growth trajectory model. Hail embryos are initialized in the hail growth module every 3 min of the radar analysis period (2251–0000 UTC) to produce over 2.7 million hail trajectories. A spatial integration technique considering all trajectories is used to identify locations within the supercell where melted particles and subsevere and severe hailstones reside in their lowest and highest concentrations. It is found that hailstones are more likely to reside for longer periods closer to the downshear updraft within the midlevel mesocyclone in a region of decelerated midlevel mesocyclonic horizontal flow, termed the downshear deceleration zone (DDZ). Additionally, clusters of trajectories are analyzed using a trajectory clustering method. Trajectory clusters show there are many trajectory pathways that result in hailstones ≥ 4.5 cm, including trajectories that begin upshear of the updraft away from ideal growth conditions and trajectories that grow within the DDZ. There are also trajectory clusters with similar shapes that experience widely different environmental and hailstone characteristics along the trajectory.

SIGNIFICANCE STATEMENT: The purpose of this study is to understand how hail grew in a thunderstorm that was observed by numerous instruments. The observations were input into a hail trajectory model to simulate hail growth. We found a part of the storm near the updraft where hailstones could remain aloft longer and therefore grow larger. Most modeled severe hailstones were found in the storm in this region. However, we also found that there are many different pathways hailstones can take to become large, although there are still some common characteristics among the pathways.

KEYWORDS: Hail; Trajectories; Supercells; Radars/Radar observations; Cloud microphysics; Cloud retrieval

---

1. Introduction

Hailstones cause extensive damage to property and agriculture across the United States every year. Improved understanding of the internal hailstorm characteristics and hailstone properties that influence hail growth, and ultimately final hailstone size at the surface, is critical for determining the eventual surface impacts of hail. During the 1970s and 1980s, many hail growth studies emerged from the National Hail Research Experiment (NHRE), the Cooperative Convective Precipitation Experiment (CCOPE; High Plains), and the National Severe Storms Laboratory (NSSL) annual spring observations of severe storms in Oklahoma (southern plains). These early field projects provided the basis for foundational work on hail growth (e.g., Heymsfield 1978; Paluch 1978; Heymsfield et al. 1980; Heymsfield 1982; Heymsfield and Musil 1982; Nelson 1983; Ziegler et al. 1983, hereafter Z83; Nelson and Knight 1987; Nelson 1987; Rasmussen and Heymsfield 1987a,b;

Miller et al. 1988, hereafter M88; Miller et al. 1990, hereafter M90; Conway and Zrnić 1993).

Studies of hail trajectories are important, as they can reveal what aspects of the storm directly influence the trajectories and impact the amount of hail growth that can take place. For example, the main updraft characteristics are important to hail formation since most trajectories traverse near or through the updraft. Early hail trajectory studies used idealized flow fields (Browning 1963; Musil 1970; English 1973) to simulate airflow and hailstone trajectories employing either 1D or 2D (spatial) time-varying kinematic and microphysical storm models to calculate hail trajectories. In the following decade, numerous multi-Doppler studies used radar-derived 3D airflow and parameterized cloud water and ice fields to grow numerically simulated hail (Paluch 1978; Heymsfield et al. 1980; Foote 1984; Heymsfield 1983; Nelson 1983; Miller and Fankhauser 1983; Z83; Knight and Knupp 1986; Nelson and Knight 1987; Nelson 1987; Rasmussen and Heymsfield 1987b; M88; M90; Conway and Zrnić 1993). These earlier observational studies applied simplifying assumptions to approximate the in-storm thermodynamic fields and hydrometeor contents. Model simulations have more recently been used to provide

internal storm characteristics for simulated hail trajectories (Adams-Selin and Ziegler 2016, hereafter ASZ16; Dennis and Kumjian 2017; Kumjian and Lombardo 2020; Lin and Kumjian 2022). The latter modeling studies have collectively identified in-storm components that contribute to hail growth under varying environmental conditions of shear and thermal stratification (e.g., CAPE), including updraft characteristics, cloud water contents, and airflow patterns. These storm morphological features modulate how long a hailstone will remain aloft in the hail growth zone (HGZ), referred to as "residence time," which is a primary control of final hailstone mass and diameter. The HGZ has been defined in various previous studies as the storm sublayer with ambient temperatures ranging from −10°C through between −25° and −40°C, possibly in part to account for complexities of variable or smaller hail sizes and fall speeds in strong updrafts (Knight et al. 1981; Nelson 1983; Z83; Foote 1984; M88; Knight and Knight 2001). The present study aims to further explore how these in-storm components, in conjunction with one another, can impact a hailstone's trajectory through the storm that could lead to longer residence times. It employs a novel, kinematically driven diabatic Lagrangian analysis (DLA) retrieval approach (Ziegler 2013a,b) to generate physically realistic in-storm fields to drive a trajectory model of hail growth.

Updraft characteristics are critical for hail production, particularly the balance between the updraft's vertical velocity and the hailstone's terminal velocity (Browning 1963; Morgan 1972; Heymsfield 1983; Nelson 1983; Miller and Fankhauser 1983; Z83; Foote 1984; Musil et al. 1986; M90; Conway and Zrnić 1993; Kennedy and Detwiler 2003; Knight and Knight 2005; Grant and van den Heever 2014). Strong updrafts inhibit hail growth by lofting small particles away from the HGZ resulting in minimal growth (Browning and Foote 1976; Nelson 1983; Foote 1984; Musil et al. 1986; Rasmussen and Heymsfield 1987b; Z83). A large area of moderate 20–40 m s^{-1} vertical velocities (a broader updraft) is an important updraft feature for significant hail growth potential (English 1973; Nelson 1983; Z83; Foote 1984; Nelson and Knight 1987; Nelson 1987; Picca and Ryzhkov 2012; Kumjian et al. 2021). Dennis and Kumjian (2017) found that the environmental hodograph can control updraft strength, width, and size. Furthermore, Lin and Kumjian (2022) found that environments with moderately large values of CAPE and precipitable water associated with broad, moderately strong updrafts and supercooled cloud water contents are supportive of large hail growth. Greater zonal deep-layer shear can elongate the updraft in the downshear direction, potentially leading to greater hail production as zonal shear increases, which often can be associated with large hail reports (Johnson and Sugden 2014; Taszarek et al. 2017). Conversely, an elongated updraft in the north–south direction is associated with less hail production as meridional shear increases (Dennis and Kumjian 2017). Wider updrafts are also associated with greater liquid water content (Peters et al. 2019, 2020; Kumjian et al. 2021) likely due to reduced lateral entrainment mixing and increased numbers of surface-based updraft air trajectories. However, Lin and Kumjian (2022) found that environments with larger values of CAPE above a moderate threshold value may be associated with less optimal storm characteristics for large hail

growth. English (1973) and Homeyer et al. (2023) both emphasize greater vertical alignment of the mesocyclone with height can lead to larger hail. Although unknowns still exist regarding controls on and impacts of updraft shape and orientation, these studies have nevertheless demonstrated that updraft characteristics are important and can impact hailstone size, as will be further addressed in this study.

Many previous studies have emphasized the importance of internal storm airflow patterns for hail growth (Browning and Foote 1976; Nelson 1983; Z83; Foote 1984; Nelson 1987). Nelson (1983) suggested that a storm's internal kinematics, particularly its updraft area aspect ratio relative to airflow path, have greater control on severe hail development than its microphysics. M88 came to a similar conclusion that variations in hail are "controlled more by effects on residence time associated with the horizontal dimension of the updraft and the orientation of the updraft with respect to the horizontal ventilating winds." Horizontal winds should be oriented to favor horizontal embryo transport across the major axis of the broad moderate updraft area (Nelson 1983) to maximize residence time within the midlevels (specifically 6–7 km) (Foote 1984) and the HGZ (Tessendorf et al. 2005). However, Nixon and Allen (2022) note that a storm's inflow-environmental kinematics (i.e., hodograph) are broadly similar among hail-producing supercells and thus do not clearly distinguish between hailstone sizes. Homeyer et al. (2023) found that storm-relative wind speed perpendicular to storm motion (above 2 km) increases as hail size increases. The relationship between hailstone size and specific environmental airflow patterns is complex and remains poorly understood. The present study explores the impact of midlevel airflow patterns on all hail produced within the storm as well as the eventual hailstone size observed at the surface. We hypothesize that the orientation of the storm-relative shear at midlevels plays a role in generating a favorable hail growth regime since the midlevel HGZ is where most hail growth occurs.

Although a subset of common hailstone trajectory pathways have been noted in the literature (e.g., Browning and Foote 1976), subsequent trajectory studies have identified a variety of additional possible pathways (Heymsfield and Musil 1982; Z83; Nelson and Knight 1987; M88; M90; Tessendorf et al. 2005). Trajectories of subembryo particle sizes have been analyzed to determine source regions for large hailstones (Browning and Foote 1976; M88; Tessendorf et al. 2005; Dennis and Kumjian 2017), although there is less knowledge on the trajectory pathways common to hailstones (particularly large hail) once larger embryos are already present. Unanswered questions remain about trajectory pathways, particularly concerning the degree of complexity of pathways that large hail trajectories can take through the storm. Improved understanding of hailstone trajectories (e.g., embryo source regions, midlevel HGZ volumes, fallout locations) could guide future hail research in helping to better identify what characteristics or subregions of hailstorms are most impactful. The present study aims to answer these questions with a novel hail trajectory dataset by further documenting how a hailstone's trajectory relates to the observed and derived in situ storm conditions.
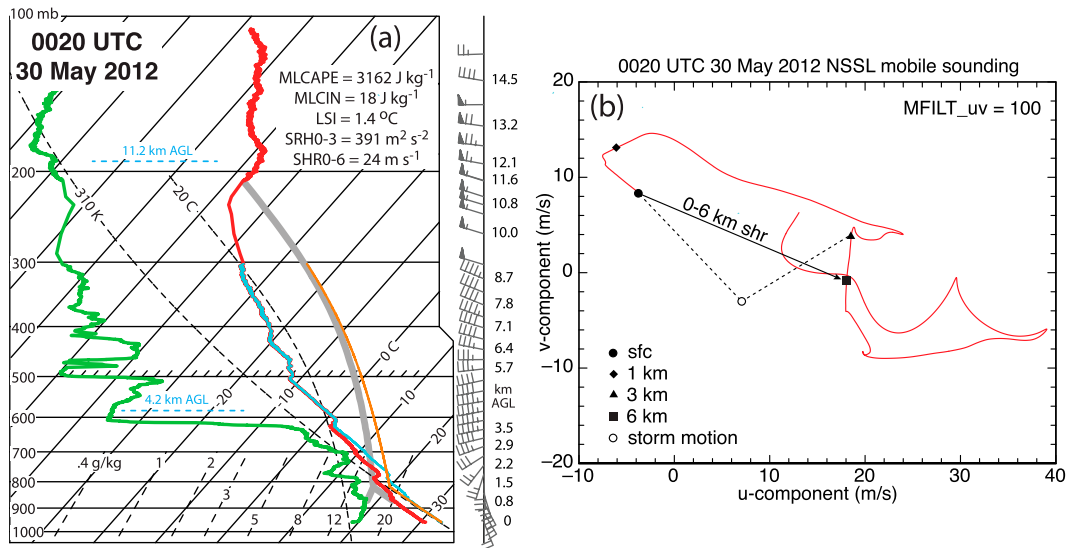
FIG. 1. Composite mobile storm-following environmental sounding on 29–30 May 2012 in the far-inflow of the Kingfisher supercell. The sounding is a composite of observations from the surface through 490 mb (1 mb = 1 hPa) in the 0020 UTC 30 May sounding with observations at pressures lower than 490 mb from the earlier 2029 UTC 29 May sounding (e.g., DiGangi et al. 2021). The sounding composite is justified by relatively weak upper-tropospheric, environmental temporal and spatial gradients and the need to remove anvil effects to more accurately estimate conserved lifted parcel thermodynamic properties. (a) Skew T–log$p$ plot with sounding parameters, including surface-based mixed-layer convective available potential energy and convective inhibition (MLCAPE and MLCIN), lid strength index (LSI), 0–3-km storm-relative helicity (SRH0–3), and 0–6-km bulk vertical wind shear (SHR0–6). The orange and cyan curves (representing the lifted-parcel and environmental virtual temperature profiles) are shown to aid visualization of MLCAPE and MLCIN values. The blue dashed lines indicate the 4.2 and 11.2 km AGL levels, the region where embryos are initialized. (b) The sounding hodograph with markers as labeled to indicate the location of 1, 3, and 6 km AGL altitudes and 0–6-km shear vector. A low-pass filter with a period of 100 s was applied to lightly smooth the wind profile (e.g., Wade et al. 2018).

2. Storm overview and data analysis methods

A hail-producing supercell near Kingfisher, Oklahoma, was sampled by multiple ground-based mobile and airborne platforms between 2251 UTC 29 May 2012 and 0000 UTC 30 May 2012 during the Deep Convective Clouds and Chemistry (DC3) field campaign (Barth et al. 2015). Observations from three mobile radars and one environmental sounding unit are used in the present study. The environmental sounding obtained at 0020 UTC 30 May is shown in Fig. 1.

a. Radar analyses

Multi-Doppler radar analyses were performed at 3-min intervals using the variational (VAR) method (Potvin et al. 2012a), as described in section 2.1 of DiGangi et al. (2016). Davenport et al. (2019) obtained very good agreement between the time-dependent Kingfisher radar-analyzed and simulated Kingfisher maximum main updraft profiles, with observed and modeled updraft maxima ranging from ∼30 m s^{-1} up to slightly over 60 m s^{-1} in the supercooled cloudy updraft layer from ∼4 to ∼12 km AGL. An observing system simulation experiment (OSSE) with emulated pseudo-radar observations of another simulated supercell storm by Potvin et al. (2012a,b) indicates expected VAR vertical velocity root-mean-square errors (RMSEs) that increase monotonically from ∼3 m s^{-1} at 4 km up to ∼12 m s^{-1}

at 12 km, broadly consistent with the (vertically bounded) vertical velocity differences of up to order 10 m s^{-1} in the same layer obtained by Davenport et al. (2019). These results are collectively equivalent to rather modest maximum 10%–16% errors normalized against maximum updraft with increasing height. Other advantages and limitations of the VAR method are described in Potvin et al. (2012a,b). Output variables (Table 1) include the Cartesian wind components (m s^{-1}) in the west–east (u), south–north (v), and vertical (z) directions and the radar reflectivity Z (dBZ) on a fixed, ground-relative radar analysis grid (90 km × 60 km × 17.5 km) with a 0.5-km grid spacing and grid origin height $z = 0.20$ km.

b. Diabatic Lagrangian analysis

Diabatic Lagrangian analysis (DLA) is an innovative technique used to retrieve the 3D, time-dependent fields of heat and water substance (Table 1) from the input 4D radar analysis data (Ziegler 2013a,b, see also DiGangi et al. 2016 and Hosek et al. 2023) that has been validated by an OSSE utilizing an earlier supercell simulation (Ziegler et al. 2010). The DLA diagnoses the rain mixing ratio q_r (g kg^{-1}), graupel/hail mixing ratio q_g (g kg^{-1}), and snow mixing ratio q_s (g kg^{-1}) via a partitioning algorithm of the radar reflectivity field. The DLA employs these diagnosed precipitation fields to predict the 3D gridpoint fields of potential temperature θ (K), water vapor mixing ratio

TABLE 1. List of radar analysis variables, diabatic Lagrangian analysis (DLA) retrieval variables, and derived variables in the hail trajectory model. Derived variables were obtained from DLA-retrieved variables using the Bolton (1980) formulas.

Variable name	Symbol	Units	Source
Cloud water mixing ratio	q_c	kg kg^{-1}	DLA
Cloud ice mixing ratio	q_i	kg kg^{-1}	DLA
Cloud droplet diameter	D_c	m	DLA (derived)
Ambient environmental air temperature	T_a	K	DLA (derived)
Ambient environmental air pressure	p_a	Pa	DLA (sounding)
u component (west–east)	u	m s^{-1}	Radar analysis
v component (south–north)	v	m s^{-1}	Radar analysis
w component (vertical)	w	m s^{-1}	Radar analysis
Reflectivity	Z	dBZ	Radar analysis
Air density	ρ_a	kg m^{-3}	DLA (derived)
Water vapor density at T_a	$\rho_{v,a}$	kg m^{-3}	DLA (derived)
Saturation vapor pressure of the ambient environmental air	$e_{s,a}$	kg m^{-1} s^{-2}	DLA (derived)

q_v (g kg^{-1}), cloud liquid water mixing ratio q_c (g kg^{-1}), and cloud ice mixing ratio q_i (g kg^{-1}). The OSSE-estimated RMSEs for retrieved cloud water mixing ratio[1] up to ~6 g kg^{-1} were on the order of ~0.3 g kg^{-1} from the DLA, along with a linearly increasing dry bias with an increasing height of up to ~16% at midlevels (Ziegler 2013a). The Kingfisher storm DLA yields up to ~12 g kg^{-1} cloud water mixing ratios by the −40°C updraft core level at 12 km (not shown), which compared to the ~14 g kg^{-1} of condensable water vapor mixing ratio in the inflow sounding below 12 km (Fig. 1) corresponds to a maximum cloud water mixing ratio of up to 86% of its adiabatic value. Most of this depletion in the DLA is due to integrated retrieved scavenging by size-distributed graupel/hail particles and raindrops along updraft air trajectories. In situ sounding analyses of strong deep convection have demonstrated that high-speed storm updraft cores are virtually undiluted by environmental air at least through storm midlevels (Davies-Jones 1974). In comparison, both Z83 and M90 assumed up to 100% adiabatic cloud liquid water profiles. Advantages, limitations, and expected accuracies of the DLA are detailed in Ziegler 2013a. The DLA has been applied in studies of the 29 May 2012 Kingfisher supercell by Yang et al. (2015), DiGangi et al. (2016), Waugh et al. (2018), Bela et al. (2018), Chmielewski et al. (2020), and DiGangi et al. (2021).

c. Storm overview

Prior analysis of the storm environment is presented in DiGangi et al. (2016), but internal storm characteristics relevant to hail formation will be briefly recapitulated here. The Kingfisher supercell's updraft was crescent shaped and was oriented with a predominantly downshear major axis for much of its life cycle (Fig. 2). The updraft was steadily strengthening but pulsed upward at approximately 2302, 2318, 2330, 2348, and 0000 UTC as indicated by transient increases in updraft mass flux (Fig. 3a) and updraft volume (DiGangi et al. 2016, their Fig. 11) relative to a linear upward trend of updraft intensity. After 2330 UTC, the updraft volume and mass flux are consistently larger for the

remainder of the analysis period. This is an important feature to note as Tessendorf et al. (2005) showed that increases in the updraft volume resulted in hail growth > 1 cm and the continued increase in the updraft volume resulted in more favorable hailstone trajectories. Following the updraft volume, the maximum graupel/hail mixing ratio (Fig. 3b) increases within the hail growth zone around each pulse and remains above 7 g kg^{-1} in the midlevels shortly after the first pulse.

3. Hail growth trajectory model

HAILCAST was originally developed by combining a time-dependent hail model with a one-dimensional steady-state cloud model (Poolman 1992), with later improvements made by Brimelow et al. (2002, 2006) and Jewell and Brimelow (2009). Limitations of using a time-dependent hail model with a one-dimensional steady-state cloud model motivated the development of WRF-HAILCAST (ASZ16). WRF-HAILCAST coupled the time-dependent hail model with a convection-allowing model (CAM) and included significant updates to the hail model physics (see ASZ16 section 2b). A major improvement of WRF-HAILCAST relative to HAILCAST was the use of CAM-simulated updraft characteristics to drive the time-dependent hail model, all of which is performed within a WRF simulation. WRF-HAILCAST was further refined as informed by its ongoing operational performance assessment during the annual NOAA Hazardous Weather Testbed Experimental Forecast Program (Adams-Selin et al. 2019, 2023). Since other versions of HAILCAST are presently being developed by other investigators, the term "ASZ16-HAILCAST" will hereafter be substituted for "HAILCAST."

The 3D, time-dependent temperature, moisture, and airflow fields from the DLA and radar analyses (Table 1) herein are input to a lightly modified version of the ASZ16-HAILCAST hail physics module (with modifications described below). The various hail growth model variables and parameters described in sections 3a–h are listed in Tables 1–3. The following growth physics are for spherical hailstones as assumed by ASZ16-HAILCAST.

---

[1] Supercooled cloud water mixing ratio is considered the most impactful microphysical storm-environmental variable on hail growth.
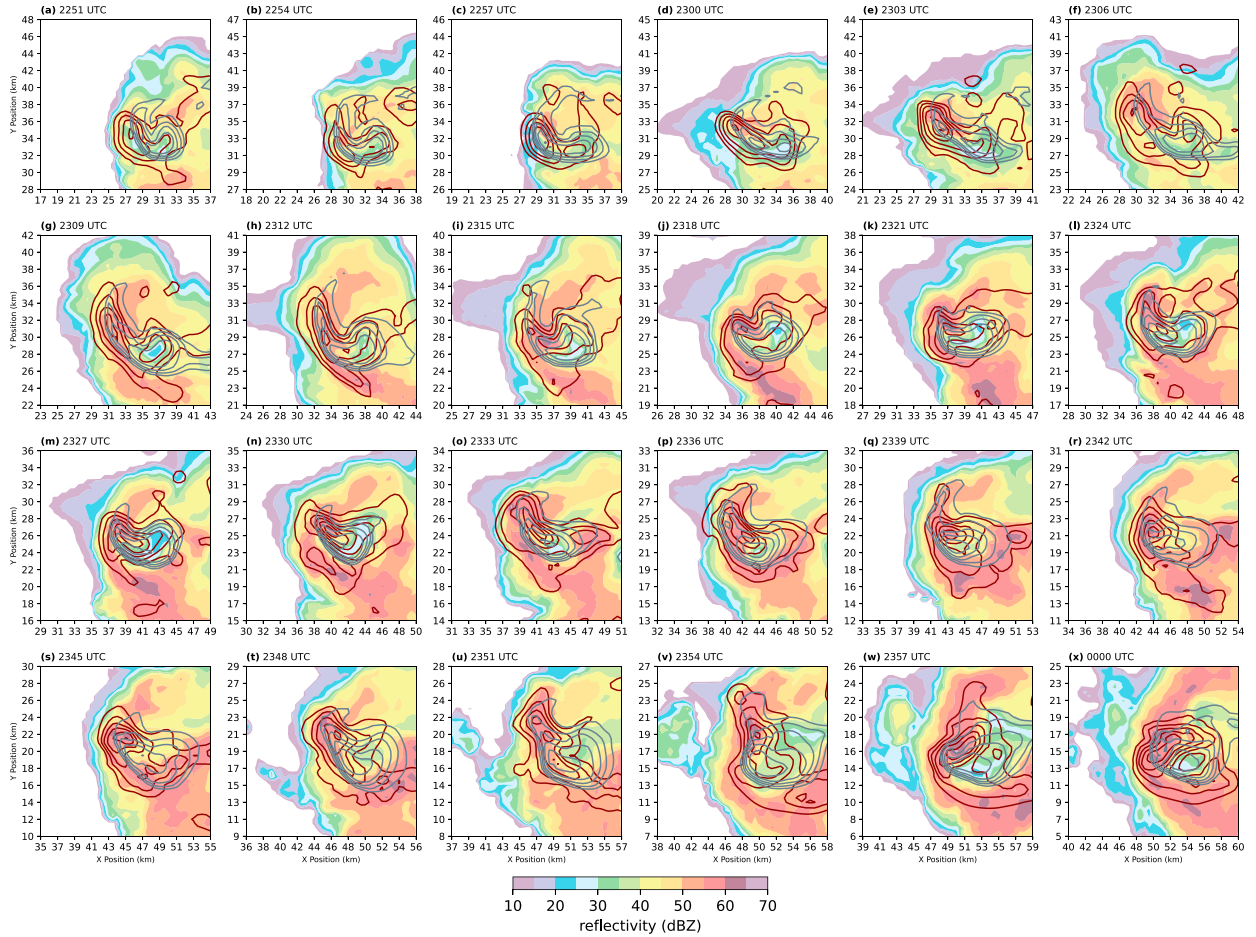
FIG. 2. (a)–(x) Embryo domain at 7.2 km AGL for all 24 radar/DLA analysis times from 2251 UTC 29 May to 0000 UTC 30 May 2012. Red contours are vertical velocity at 10 m s^{-1} beginning at 10 m s^{-1} intervals and gray contours are q_c contoured at 2 g kg^{-1} intervals starting at 2 g kg^{-1}. The shaded regions are reflectivity contoured at 5-dBZ intervals beginning at 10 dBZ. The 3D embryo search domain is dimensioned 20 km × 20 km horizontally, from 4.2 to 11.2 km AGL vertically, and is approximately centered in the main updraft. The embryo grid spacing is 0.25 km in all directions. The embryo domain moves south and east following the storm motion at rates of 1 km (3 min)$^{-1}$. Hail trajectories are initialized at any embryo grid point with reflectivity exceeding 20 dBZ.

a. Hailstone terminal velocity

The hailstone terminal velocity or fall speed V_t (m s^{-1}; Table 2) is calculated via a dependence on the Reynolds number (Re$_X$) using methods from Rasmussen and Heymsfield (1987a, hereafter referred to as RH87a), as also applied in the ASZ16-HAILCAST model. The terminal velocity is calculated from an expression of the following form (RH87a):

$$V_t = \frac{\nu_d \text{Re}_X}{\rho_a D}, \quad (1)$$

where Re$_X = (X/C_D)^{0.5}$ is the Reynolds number, $X = 8mg\rho_a/[\pi(\nu_d)^2]$ is the Best number, C_D is the drag coefficient, ν_d is the dynamic viscosity of air (Table 3), ρ_a is the density of air, D is the hail diameter (m), m is the mass of the hailstone (kg), and g is the gravitational acceleration (m s^{-2}). The dynamic viscosity is calculated via

$$\nu_d = 1.718 \times 10^{-5} \left(\frac{393.155}{T_a + 120} \right) \left(\frac{T_a}{273.155} \right)^{3/2}, \quad (2)$$

where T_a is the ambient environmental air temperature (K). RH87a computed Re$_X$ as a function of empirical fits to the Best number X spanning four prescribed X subranges. The four Best–Reynolds number relationships provided in Eqs. (B1)–(B4) of RH87a were based on a drag coefficient C_D value of 0.6 for Eq. (B4) and smooth spheres for Re$_X \le 30$ (see their Fig. 3). To avoid undefined numbers, a slight correction was made to Eq. (B1) in the following form:

$$\log_{10} \text{Re}_x = -1.7095 + 1.334\,38 \log_{10} X - 0.115\,91 (\log_{10} X)^2,$$

at all points where $X < 500$. Further explanation of the methodology and V_t equations can be found in appendix B of RH87a and section 2b of M88.
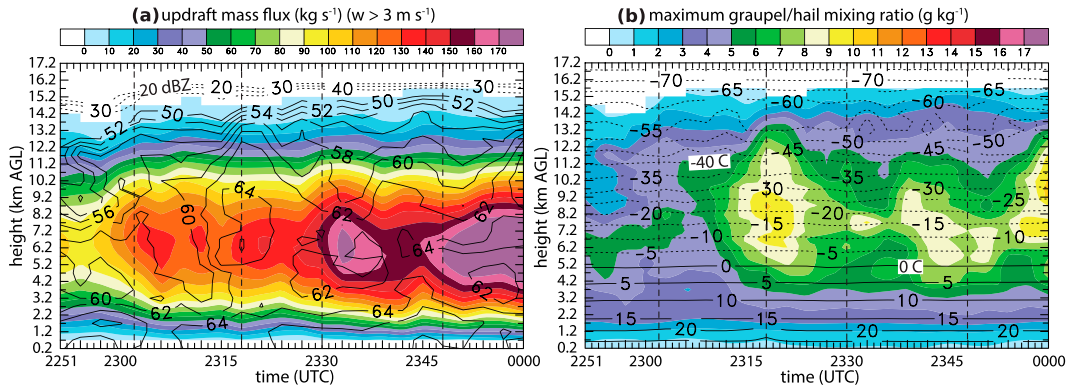
FIG. 3. Time series of (a) horizontally integrated updraft mass flux (kg s^{-1}) exceeding 3 m s^{-1} with reflectivity contours, and (b) maximum graupel/hail mixing ratio (g kg^{-1}) with contours of maximum of main updraft or ambient temperature during the analysis period (2251–0000 UTC). Dashed vertical lines indicated where the updraft pulsed upward according to DiGangi et al. (2016).

b. Collection of cloud water

Collection of supercooled liquid water provides the main mass source of growth in hailstones, although the amount of collection can vary depending on several factors including growth regime. For both dry growth (i.e., all accreted water is frozen on the surface of the hailstone) and wet growth (i.e., only a fraction of accreted water is frozen, with the unfrozen water either soaking into the hailstone or remaining unfrozen on the surface), the mass rate of change due to collection of supercooled water (i.e., accretion) takes the following form:

$$\left(\frac{dm}{dt}\right)_{\text{water}} = \frac{\pi}{4}D^2 V_t q_c E_{\text{cw}}, \qquad (3)$$

where q_c is the cloud water mixing ratio and E_{cw} is the cloud water collection efficiency. The falling hailstone sweeps out cloud droplets within the cylindrical volume equal to the horizontal circular hailstone area multiplied by the fall distance $V_t \Delta t$, where the hail growth model time step $\Delta t = 1$ s. The collection efficiency of cloud water droplets E_{cw} during sweepout to a good approximation is conventionally assumed to have a value of unity (e.g., Z83). The density of the rimed layer in dry growth is determined via the empirically derived hail ice layer density ρ_l, cloud droplet diameter D_c, hailstone impact velocity V_{imp}, and temperature T_s as described in Heymsfield and Pflaum (1985) and ASZ16. Impact velocity was calculated via a linear interpolation between the four Reynolds number, Stokes number, terminal velocity,

TABLE 2. List of parameters and variables related to physical hail characteristics in the hail trajectory model.

Variable name	Symbol	Units	Value
Hailstone diameter	D	m	
Equivalent spherical volume diameter	D_{eq}	m	
Hailstone maximum dimension	D_{max}	m	
Hailstone water fraction	F_w	Unitless	
Hailstone mass	m	kg	
Surface water shell mass	M_{sfc}	kg	
Surface water shell mass threshold	M_{wcrit}	kg	1×10^{-10}
Prandtl number	Pr	Unitless	0.71
Reynolds number	Re	Unitless	
Reynolds number (Best number relationship)	Re$_X$	Unitless	
Schmidt number	Sc	Unitless	0.60
Hailstone surface temperature	T_s	K	
Hailstone terminal velocity	V_t	m s^{-1}	
Volume	V	m^3	
Hailstone impact velocity	V_{imp}	m s^{-1}	
Best number	X	Unitless	
Change in hailstone mass since last time step	Δm	kg	
Hailstone mass growth due to ice accretion during time step	Δm_i	kg	
Hailstone heat content change during time step	Δq	kg	
Bulk hail density	ρ_h	kg m^{-3}	
Hail ice layer density	ρ_l	kg m^{-3}	

TABLE 3. List of dynamical, thermodynamical, and microphysical parameters and variables in the hail trajectory model.

Variable name	Symbol	Units	Value
Drag coefficient	C_D	Unitless	
Specific heat capacity of ice	$c_{p,i}$	J kg^{-1} K^{-1}	2093
Specific heat capacity of water	$c_{p,w}$	J kg^{-1} K^{-1}	4182
Diffusivity of water vapor in air	D_v	m^2 s^{-1}	
Saturation vapor pressure at the hailstone surface	$e_{s,s}$		
Cloud water collection efficiency	$E_{\rm cw}$	Unitless	
Cloud ice collection efficiency	$E_{\rm ci}$	Unitless	
Mean ventilation coefficient for heat	$\overline{f_H}$	Unitless	
Water vapor ventilation coefficient	$\overline{f_v}$	Unitless	
Gravitational acceleration	g	m s^{-2}	9.8
Thermal conductivity of air	k_a	J m^{-2} s^{-1}	
Latent heat of vaporization	L_e	J kg^{-1}	2.499×10^6
Latent heat of melting	L_m	J kg^{-1}	2.833×10^6
Gas constant for water vapor	R_v	J kg^{-1} K^{-1}	461.48
Temperature difference between ambient air and equilibrium state at the hailstone surface	ΔT	K	
Vapor density difference between ambient air and equilibrium state at the hailstone surface	$\Delta \rho$	kg m^{-3}	
Water vapor density at T_s	$\rho_{v,s}$	kg m^{-3}	
Dynamic viscosity of air	ν_d	kg m^{-1} s^{-1}	
Kinematic viscosity of air	ν	m^2 s^{-1}	1.252×10^{-5}
Heat transfer coefficient	χ	Unitless	

and impact velocity relationships presented in Eqs. (7)–(10) of Rasmussen and Heymsfield (1985).

All collected supercooled cloud water is frozen during dry growth, whereas only a fraction F_w of the collected cloud water remains unfrozen during wet growth while the remaining fraction $(1 - F_w)$ freezes. The unfrozen collected cloud water can either soak into previously porous rime if the hailstone bulk density is less than that of solid ice (assumed to be 900 kg m^{-3}) following Z83, or else can collect in a surface water shell if the hailstone is at solid-ice density. Although ASZ16-HAILCAST assumed that shedding of excess water can occur if the surface water shell mass $M_{\rm sfc}$ (kg) exceeds a threshold value $M_{\rm sfc} = M_{\rm wcrit} = 1 \times 10^{-4}$ kg (see ASZ16 for discussion), a smaller default fixed value of $M_{\rm wcrit} = 1 \times 10^{-10}$ kg is assumed to represent a thinner water layer, although sensitivity tests of the shedding threshold will be considered in future work. For wet growth, the ice layer density is set to 900 kg m^{-3}. The bulk hail density during wet growth is updated by dividing the volume of the hailstone by the mass of the hailstone that includes any soaked water.

Neither raindrop nor snow mass collection rates are considered by the present hailstone growth model (e.g., Z83). Although Kumjian and Lombardo (2020) suggest that raindrop collection may be a nonnegligible source of hailstone mass under certain ideal circumstances, demonstrating a plausible hypothetical role of raindrop collection would require either laboratory or detailed numerical model data on the collection efficiency of raindrops by hailstones which presently do not exist. Due to the rather large impact velocities of hailstones and raindrops, and the aforementioned lack of reliable data to prescribe raindrop collection efficiency, splashing raindrop collisions could conceivably result in loss of an appreciable but unknown fraction of intercepted raindrop mass. Similarly, for a dry hailstone surface, the large impact momentum difference would likely result in snow particle shattering and rebound of the small collision fragments. Furthermore, both raindrops and snow particles are also

in extremely low total concentrations relative to cloud droplets, thus limiting effective raindrop–hail and snow–hail collision rates (e.g., Knight and Knight 1970; Ziegler 1985, 1988; Knight et al. 2008). These processes could have implications of hailstone surface characteristics and therefore should be investigated in future work.

c. Collection of cloud ice

Similar to the mass rate of change due to the collection of cloud water, the mass rate of change due to the collection of cloud ice takes the following form:

$$\left(\frac{dm}{dt}\right)_{\rm cloud\text{-}ice} = \frac{\pi}{4} D^2 V_t q_i E_{\rm ci}, \qquad (4)$$

where q_i is the cloud ice mixing ratio and $E_{\rm ci}$ is the cloud ice collection efficiency. In several previously developed hail growth models (e.g., ASZ16), $E_{\rm ci}$ has been assumed to be dependent of the hailstone surface temperature T_s. It is conventionally assumed that $E_{\rm ci}$ has a unit value if the ambient environmental temperature T_a is at or above 0°C, whereas $E_{\rm ci}$ is assumed to be zero at or below -40°C (e.g., ASZ16). For hailstone temperature T_s ranging between 0° and -40°C, $E_{\rm ci}$ takes the linear functional form:

$$E_{\rm ci} = 1 - \frac{273.155 - T_s}{40}, \qquad (5)$$

which substitutes T_s for T_a in the analogous E_{cx} expression of Z83.

d. Vapor diffusion

Vapor growth or decay via deposition or sublimation, respectively, which follows Eq. (4) of ASZ16 as adapted from RH87a and Pruppacher and Klett (1997), takes the following form:

$$\left(\frac{dm}{dt}\right)_{\text{vapor}} = \frac{2\pi D \overline{f_v} D_v}{R_v}\left(\frac{e_{s,a}}{T_a} - \frac{e_{s,s}}{T_s}\right), \qquad (6)$$

where $\overline{f_v}$ is the water vapor ventilation coefficient, the water vapor diffusivity in air $D_v = 0.226 \times 10^{-4}\,(T/T_0)^{1.81}\,(10^5/p_a)$ (Pruppacher and Klett 1997), R_v is the gas constant for water vapor, and $e_{s,a}$ and $e_{s,s}$ are the saturation vapor pressures of the ambient environmental air and at the hailstone surface, respectively. The values of $\overline{f_v}$ and D_v were obtained from Table A1 of RH87a. If vapor deposition is the main source of growth, the solid-ice layer density in the time step is set to 900 kg m^{-3}.

e. Heat balance condition (dry growth)

When a hailstone grows at subfreezing temperatures, the released latent heat of freezing is distributed between the hailstone and the ambient air. To account for the physical changes occurring due to freezing, a set of equations are used to determine the heat balance of the growing hailstone. The employed heat balance equations were adapted by Poolman (1992), Brimelow et al. (2002), and ASZ16 from Table 1 and Eqs. (3)–(5) of RH87a. All empirical relationships derived in RH87a adopted calorie-gram-second units with temperature (°C) and length (cm) (i.e., CGS units). The present model subsequently converts all RH87a-formulated quantities to joule-kilogram-second units with temperature expressed in kelvins and length in meters (i.e., MKS units) as required to maintain SI units of predicted quantities. For simplicity in the remainder of the section, all relationships discussed assume the latter system of units unless explicitly stated otherwise.

The temperature of the surface of the hailstone during dry growth is determined via an expression of the following form:

$$(T_s)t = (T_s)t - \Delta t\left(\frac{m - \Delta m}{m}\right) + \frac{\Delta t}{mc_{p,i}}\left[\frac{\Delta q}{\Delta t}\right] + \frac{\Delta m_w L_m}{mc_{p,i}}, \quad (7)$$

where Δm is the change in hailstone mass since the last time step, Δq is the change in heat content since the last time step, L_m is the latent heat of melting, and $c_{p,i}$ is the specific heat capacity of ice. Within this equation, the first term represents the previous hailstone temperature per unit mass, the second term the change in temperature due to the release of latent heat, and the third term the change in temperature due to the accretion of new mass. The $\Delta q/\Delta t$ term in square brackets can be replaced by Eqs. (3)–(5) of RH87a, resulting in a modified hailstone temperature expression of the following form:

$$(T_s)t = (T_s)t - \Delta t\left(\frac{m - \Delta m}{m}\right)$$
$$+ \frac{\Delta t}{mc_{p,i}}\Big[2\pi D\overline{f_H}k_a(T_a - T_s) - \overline{f_v}L_e D_v(\rho_{v,s} - \rho_{v,a})$$
$$+ \frac{\Delta m_w}{\Delta t}(c_{p,w}T_a) + \frac{\Delta m_i}{\Delta t}(c_{p,i}T_a)\Big] + \frac{\Delta m_w L_m}{mc_{p,i}}, \quad (8)$$

where $\overline{f_H}$ is the mean ventilation coefficient for heat, k_a is the thermal conductivity of air, L_e is the latent heat of vaporization, $\rho_{v,s}$ is the water vapor density at the hailstone surface, $\rho_{v,a}$ is the water vapor density at T_a in ambient air, $c_{p,w}$ is the heat capacity

of water, and Δm_i is the growth in hailstone mass due to ice accretion since the last time step. The $(\Delta m_i/\Delta t)(c_{p,i}T_a)$ term, although not included by RH87a, was added by ASZ16 to account for heat transfer due to accreted ice.

The $\overline{f_H}$ and $\overline{f_v}$ terms in the vapor diffusion and surface temperature expressions [Eq. (6) and Eq. (8), respectively] encapsulate all additional dependencies in the heat transfer equations (3)–(5) in Table 1 of RH87a, as defined by Poolman (1992) and Brimelow et al. (2002), and include the Reynolds (Re), Prandtl (Pr), and Schmidt (Sc) numbers as well as the heat transfer coefficient χ. The Re dependency of the RH87a heat transfer equations is incorporated into the heat ventilation coefficient calculation, taking the following form:

$$\overline{f_H} = \begin{cases} 0.78 + 0.308\,\text{Pr}^{1/3}\text{Re}^{1/3}, & \text{Re} < 6\times 10^3 \\ \chi_1\text{Pr}^{1/3}\text{Re}^{1/3}, & 6\times 10^3 \le \text{Re} \le 2\times 10^4 \\ \chi_2\text{Pr}^{1/3}\text{Re}^{1/3}, & \text{Re} > 2\times 10^4 \end{cases}, \quad (9)$$

where $\text{Re} = DV_t/\nu$ is the Reynolds number, ν is the kinematic air viscosity, and $\chi_1 = 0.76$ while $\chi_2 = 0.57 + 9.0\times 10^{-6}\,\text{Re}$ [Eqs. (4) and (5) of RH87a]. Although the latter Re definition differs from the Re_x expressions in the terminal velocity calculations of RH87a (section 3a), the resulting computational differences of Re are minimal for the temperature ranges encountered here.

If the hailstone is in the dry growth regime and all the accreted supercooled cloud water can be frozen, the hailstone remains in dry growth. Otherwise, if not all of the accreted supercooled cloud water can be frozen, a transition to wet growth occurs.

f. Heat balance condition (wet growth)

If the hailstone is in the wet growth regime at subfreezing temperatures, T_s remains at 0°C. The water fraction of the total hailstone mass F_w is the predicted variable. Similarly to the dry growth hailstone surface temperature calculation, the expression for water fraction F_w takes the following form:

$$(F_w)t = (F_w)t - \Delta t\left(\frac{m - \Delta m}{m}\right) + \frac{\Delta t}{mL_m}\left[\frac{\Delta q}{\Delta t}\right] + \frac{\Delta m_w}{m}. \quad (10)$$

These three terms can be interpreted as the water fraction of the hailstone before adding the mass Δm, the depletion of water fraction due to water layer freezing (as regulated by the heat transfer process), and the change in water fraction due to accretion of liquid cloud water. With the substitution of the bracketed $\Delta q/\Delta t$ term from RH87a as in section 3e, the wet growth water fraction expression takes the final form:

$$(F_w)t = (F_w)t - \Delta t\left(\frac{m - \Delta m}{m}\right)$$
$$+ \frac{\Delta t}{mL_m}\Big[2\pi D\overline{f_H}k_a(T_a) - 2\pi D\overline{f_v}L_e D_v(\rho_{v,a} - \rho_{v,0})$$
$$+ \frac{\Delta m_w}{\Delta t}(c_{p,w}T_a) + \frac{\Delta m_i}{\Delta t}(c_{p,i}T_a)\Big] + \frac{\Delta m_w}{m}. \quad (11)$$

Note that the temperature of the hailstone here is assumed to be 0°C during wet growth. If all of the retained water has

frozen, the hailstone is transitioned from wet growth to dry growth.

g. Melting

Hail melting may occur if T_a is above freezing. During the melting phase, T_s remains at 0°C. With the substitution of $D = 2r$ (where r is the hailstone radius), the heat transfer rate h for a melting hailstone [Eq. (1) of Goyer et al. (1969), hereinafter referred to as G69] takes the following form:

$$h = \frac{\chi(Pr^{1/3}k_a\Delta T + Sc^{1/3}L_eD_v\Delta\rho)Re^{1/2}}{D}, \quad (12)$$

where $\chi = \chi_1 = 0.76$ [Eq. (4) of RH87a], ΔT and $\Delta\rho$ are the difference of temperature and vapor density, respectively, between the ambient air and the equilibrium state at the hailstone surface, Pr is the Prandtl number, and Sc is the Schmidt number. For melting only, Pr and Sc are assumed a constant 0.85 (G69) rather than explicit calculation (RH87a). While the explicit calculation of these values is computed for growth rates, the impact of the relatively small variations in these values on melting rates can be neglected for computational efficiency. The thermal melting rate equation from G69 [their Eq. (3)] is the first two terms in Eq. (13) below, with the substitution of $D = 2r$. However, a cloud water collection melting rate term sourced from RH87a is also added [rightmost term in Eq. (13)] to ensure enhanced melting due to collision with cloud droplets warmer than 0°C is accounted for. The total mass melting rate $(dm/dt)_{melt}$ takes the general form:

$$\left(\frac{dm}{dt}\right)_{melt} = -\frac{\pi D^2 h}{L_m} + 0.85\pi DD_v\Delta\rho Re^{0.5} + \frac{\Delta m_w}{\Delta t}(c_{p,w}T_a)\Big/L_m. \quad (13)$$

Following Lesins and List (1986) who effectively computed the average drag coefficient $\overline{C_D}$ according to the equivalent spherical volume diameter D_{eq} for their oblate spheroidal laboratory-grown hailstones, the present melting formulation assumes $D = D_{eq}$.

The $\Delta\rho$ term can make an important contribution to the net hail melting rate in dry ambient air, as evaporation from the water surface offsets forced convective heat transfer from the air to the hailstone surface (G69). It is important to note that whereas G69 made several simplifying assumptions in their hail melting expression by assuming picked values of χ, Pr, and Sc, the present hail model evaluates the general forms of Eqs. (12) and (13) to allow the latter parameters to vary according to physical principles. The F_w value, which may vary with changing surface water mass during melting, is balanced between shedding loss and meltwater increase during each time step. Excess surface hailstone water mass exceeding M_{wcrit} is immediately shed.

h. Computational algorithm for hailstone trajectories

The first stage of the hail trajectory integration process during each time step begins with the computation of V_t and interpolation of the u, v, and w wind components and reflectivity Z (Table 3) from the 4D radar analyses to the Lagrangian point.

The hail trajectory coordinates (x, y, z) are then integrated forward by one time step via the system:

$$x_t = x_{t-\Delta t} + u\Delta t, \quad (14a)$$

$$y_t = y_{t-\Delta t} + v\Delta t, \quad (14b)$$

$$z_t = z_{t-\Delta t} + (w - V_t)\Delta t, \quad (14c)$$

where $(\Delta x, \Delta y, \Delta z)_{\Delta t} = (u\Delta t, v\Delta t, [w - V_t]\Delta t)$ is the temporal change of the ground-relative coordinates of the hailstone Lagrangian point with respect to the radar analysis grid domain during the time step, and fall speed V_t is positive (directed downward).

Following the integration of Eqs. (14a)–(14c), the second stage of the hail trajectory integration process is the interpolation of the DLA-retrieved four-dimensional θ, q_v, q_c, and q_x fields to the updated Lagrangian point. Additional thermal and microphysical parameters required by the subsequent hail physics calculations are then derived from the interpolated DLA variables.

The spatiotemporal interpolation of airflow and DLA fields to the hailstone trajectory includes storm motion effects (Ziegler 2013a,b). When performing the interpolation for each point along a hailstone's path, correction of the airflow and DLA fields for storm motion is applied first, followed by trilinear spatial and then linear temporal interpolation from bracketing analysis grid points and times. For hailstone trajectories still aloft after the final analysis time (0000 UTC 30 May 2012), the 3D wind fields are assumed to be steady state with the storm moving at the same speed observed prior to 0000 UTC. If the hailstone trajectory moves outside the DLA or radar analysis domains, the ambient environmental conditions are approximated from the base-state sounding with assumed zero hydrometeor content.

In the final stage of the hail trajectory integration process, the incremental hailstone mass and volume changes, heat budget, hailstone temperature, water fraction, and growth mode from the various hail physics terms are calculated. If $T_a > 0°C$, the hailstone mass rates of change from melting (including heat transfer from cloud collection) and breakup are then calculated. Alternately if $T_a \le 0°C$, the hailstone mass rates of change from cloud water collection, cloud ice collection, and vapor diffusion are then calculated. After updating the hailstone T_s and F_w based on the calculated heat budget (including determination of dry or wet growth mode), the hailstone mass rate of change from water shedding is then calculated. The hail trajectory model enables the diagnosis of bulk density by carrying predicted hailstone mass m and volume V as independent variables, from which bulk density $\rho_h = m/V$ is updated (Nelson 1983; Z83; Mansell et al. 2010; ASZ16). The separately determined mass and volume changes of the hailstone for each growth or decay process are incrementally applied during each time step to update the hailstone mass and volume and derive the updated hailstone bulk density.

i. Initialization and integration of hailstone trajectories

Hail trajectories are initialized within a 3D domain at individual grid points (Fig. 2) with prescribed embryo diameter and bulk density. The chosen embryo domain location is consistent with

prior research that identified the main embryo source regions and fully encompasses all areas around the main updraft (e.g., Z83; Dennis and Kumjian 2017). Although Z83 and ASZ16 employed multiple millimetric-diameter embryo sizes following conventional practice, an initial density of 500 kg m^{-3} and an initial diameter of 7 mm are chosen based on hail growth model sensitivity tests in the latter studies. Additional embryo sizes could be used, but different embryo sizes would not represent a different embryo evolution, but rather a different point in time of the embryo's development. For the purpose of this study, 7-mm embryos are sufficient as they are realistically sized graupel particles found within supercells that are likely to result in a hailstone. Given highly variable storm airflow and the nonlinear nature of hail growth, embryos are instead initialized at 250-m spacing, a finer spatial scale than previous trajectory studies. Airborne in situ measurements (Heymsfield and Musil 1982), microphysical retrievals by Ziegler (1985, 1988) and Ziegler et al. (1991; including in situ sailplane measurements of the graupel size distribution), and in situ videosonde observations of the Kingfisher storm by Waugh et al. (2018) collectively provide ample evidence of abundant, large graupel particles at altitude in midlatitude convective storms. Given the present rather dense hail trajectory calculations relative to the very broad supercell main updraft, and since expected updraft and cloud water mixing ratio errors likely vary somewhat positively or negatively in proportion to expected vertical velocity and cloud water RMSEs (see sections 2a and 2b), individual model hailstones likely encounter broadly similar mean updraft strengths and cloud contents in the supercooled liquid-cloudy updraft growth region.

The combined hail trajectory dataset thus created includes forward hail trajectories computed from each radar analysis time (3-min intervals) between 2251 and 0000 UTC (24 total analysis times). Trajectories are initialized within a 20 km × 20 km domain where at least reflectivities of 20 dBZ are present. Combining output from all 24 analysis times to complete our dataset, the total 4D dataset exceeds 2.7 million hail trajectories.

4. Results: Relation of evolving hail field structure to storm morphology

a. Evolving spatial hailstone concentration fields

Of the 2.7 million hailstone trajectories, a majority (>95%) melted completely before reaching the surface. Trajectories are categorized by final characteristic: 1) melted before reaching the surface ("melted particles"); 2) reached the surface as hailstones or graupel at subsevere limits (<2.5 cm) ("subsevere"); and 3) reached the surface as severe hailstones (≥2.5 cm) ("severe"). In the following results, the counts of embryos initialized at a particular analysis time and time-varying hailstones initialized prior to that analysis time are summed within 1 km × 1 km × 1 km cells spanning the analysis domain. For example, the 2257 UTC analysis time would include trajectories initialized at 2257 UTC at their initial position, trajectories initialized at 2254 UTC at their position 3 min into their trajectory, and trajectories initialized at 2251 UTC at their position 6 min into their trajectory (excluding trajectories that had reached ground prior to 2257 UTC). These analyses thus provide instantaneous 3D fields of the total simulated hail concentrations present in the storm at each of the 24 analysis times. The analyses at 2300 UTC (Fig. 4), 2315 UTC (Fig. 5), 2330 UTC (Fig. 6), 2345 UTC (Fig. 7), and 0000 UTC (Fig. 8) are highlighted to examine how the storm's vertical velocities, updraft shape, horizontal airflow patterns, reflectivity, and microphysical structure impact the 3D hailstone field within the storm.

Melted particle concentrations are relatively small within the regions where vertical velocities above 20 m s^{-1} are observed (Figs. 4a,b–8a,b), due to their trajectories being characterized by limited mass growth in weak updrafts and small terminal velocities that increase melting duration leading to complete melting above ground. The ubiquitous supercell bounded weak echo region (BWER) is apparent where larger vertical velocities exist, surpassing hailstone terminal velocities resulting in a region lacking numerous smaller radar-reflective particles (Figs. 4a–8a). The melted particles are not collocated with the prime growth region (discussion in section 4b); thus, minimal growth occurs.

The embryos that make up the melted particles are likely sourced near the "upwind stagnation zone" (Nelson 1983; M88; Tessendorf et al. 2005), upshear of the updraft where flow diverges around the midlevel updraft, and then are advected east by westerly horizontal flow in the midlevels. The particles found in this region make up an embryo source region coined the "embryo curtain" (Browning and Foote 1976), in which the development of the embryo curtain is described by the first two stages of growth in the Browning and Foote (1976) conceptual model. Similar to those shown in M88 and Nelson (1983), melted particles initialized north to northwest (south to southwest) of the updraft are advected anticyclonically (cyclonically) within the midlevel flow around the updraft either toward its northeast (Waugh et al. 2018) or southeast, respectively (Figs. 4a–8a). Though Grant and van den Heever (2014) hypothesize that hailstones initialized in this region can have longer residence times, as hailstones can experience greater growth prior to being advected either cyclonically or anticyclonically around the mesocyclone. Despite being advected around the mesocyclone, these embryos likely result in melted particles due to their distance from the main updraft, as compared to embryos advected around the mesocyclone close to the updraft.

Horizontal flow becomes southerly with decreasing height, resulting in the advection of melted particles further north as they are descending (not shown). For this reason, the highest concentration of melted particles is located northeast of the updraft throughout the analysis period (Figs. 4a–8a), which can also be seen denoted in Fig. 4a. M88 noted that the high reflectivities east-northeast of the updraft were likely due to melted hailstones, in agreement with the location of the highest melted particles here being collocated with the highest reflectivities (Figs. 4a,b–8a,b). The melted particles permeate a large volume possessing reflectivities typically up to or exceeding 30 dBZ at all analysis times (Figs. 7), consistent with Waugh et al. (2018) who demonstrated from in situ precipitation observations and T-matrix calculations that graupel and hail particles dominate moderate to high reflectivities. The subsevere and severe hailstones occupy much smaller volumes with smaller concentrations than melted particles, consistent with the predominance of graupel meltwater rainfall in
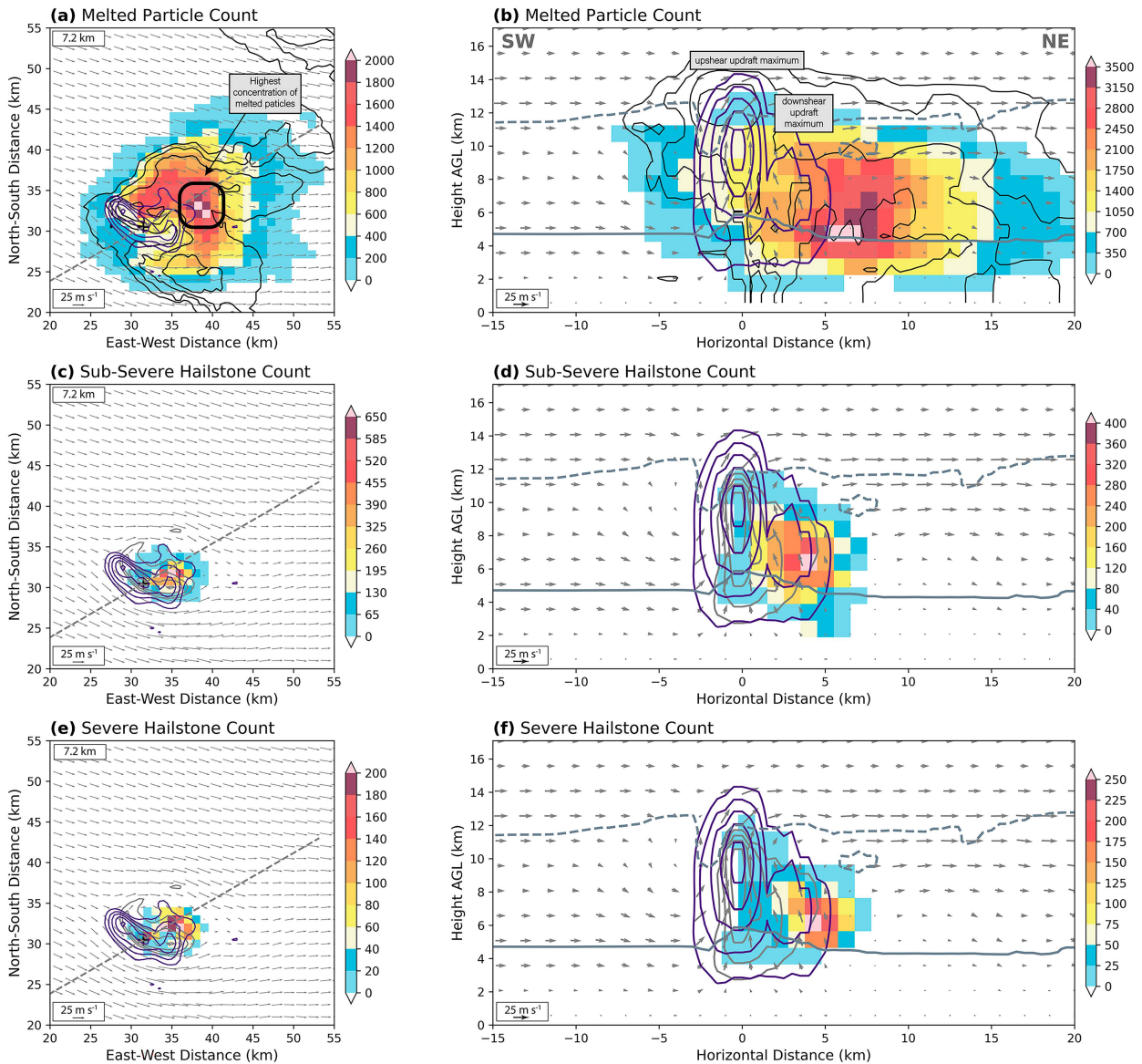
FIG. 4. Modeled concentrations of (a),(b) hail particles that completely melt above ground; (c),(d) subsevere hailstones that reach ground; and (e),(f) severe hailstones that reach ground in the Kingfisher storm at 2300 UTC. (left) Hailstone counts in a 1 km × 1 km grid cell in the *x–y* plane integrated through the full radar analysis domain depth. Ground relative horizontal in (a), (c), and (e) and horizontal along the cross section and vertical in (b), (d), and (f) wind vectors at 7.2 km (AGL) are denoted by the gray arrows. Black contours are reflectivity starting at 20 dBZ at 10-dBZ increments at 7.2 km in (a) and (b), and gray contours are q_c starting at 2 g kg^{-1} in 2 g kg^{-1} intervals. Purple contours are vertical velocity starting at 10 m s^{-1} at 10 m s^{-1} increments at 7.2 km. A black "x" is shown where the maximum of the mean vertical velocity at all levels is found. A dashed black line denotes the cross section shown directly to the right of the panel. (right) Hailstone counts in a 1 km × 1 km grid cell in the corresponding cross section, where grid cells are horizontally integrated across the full radar analysis domain in the direction normal to the cross section. The dashed gray line indicates the −40°C level and the solid gray line indicates the 0°C level.

midlatitude convective storms (e.g., Ziegler 1988) and the lower probabilities of severe and large hail.

The updraft resembles a crescent shape for a majority of the analysis period, with two distinct updraft cores (Fig. 2). The stronger updraft maximum is located to the northwest or upshear updraft core flank ("upshear updraft maximum"), while the weaker updraft maximum is located to the southeast on the downshear

flank ("downshear updraft maximum") (see Fig. 6b for annotation). Vertical velocities within both updraft cores are too strong for the terminal velocity of hailstones to maintain the quasi-balance needed to extend residence time and grow (at least initially in their life cycle), but this balance is supported along the edges of the downshear updraft maximum within the midlevel mesocyclone centered around 7 km AGL (Figs. 4–8). Large
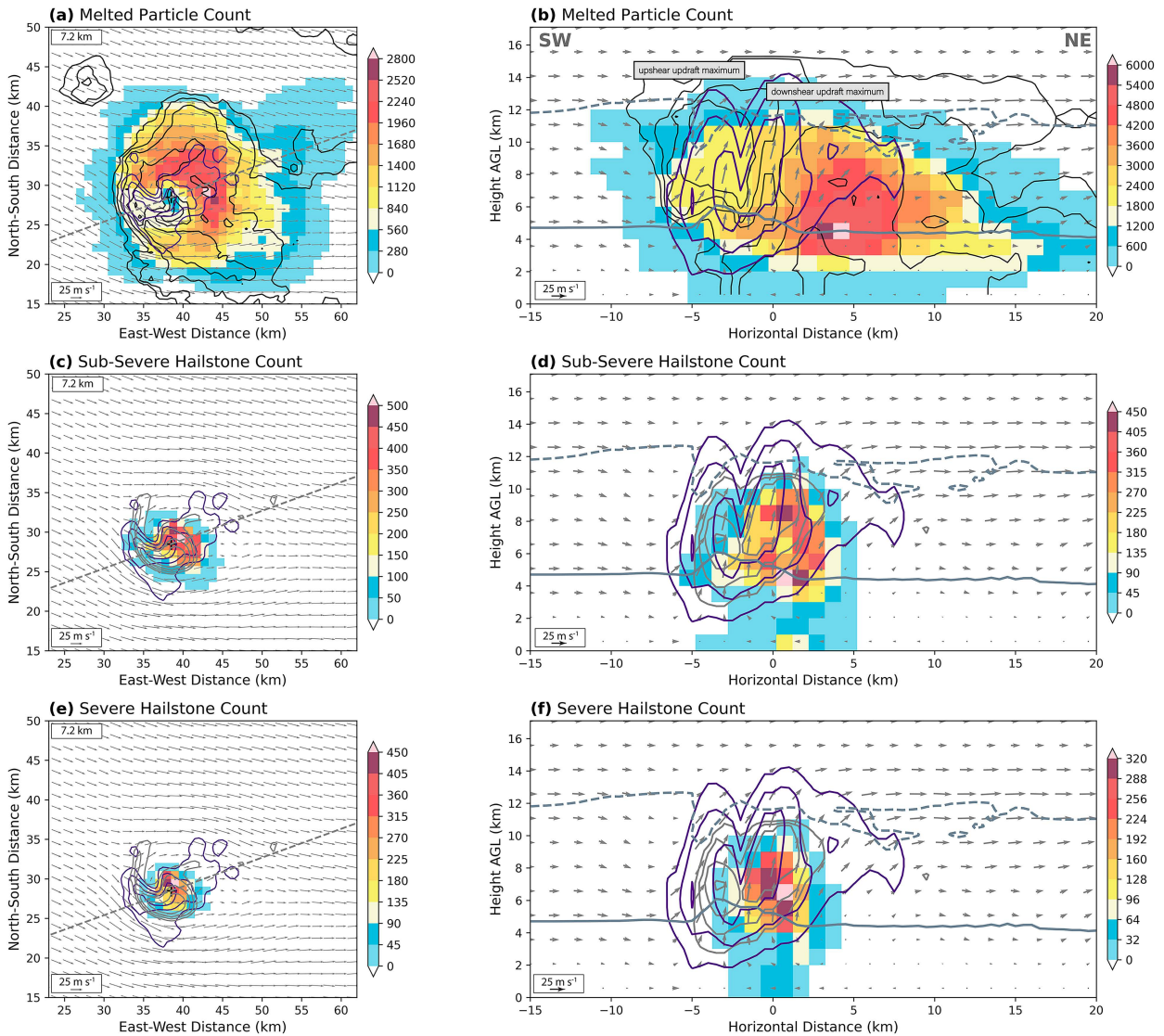
FIG. 5. As in Fig. 4, but at 2315 UTC.

cloud liquid water contents are observed within all portions of the downshear updraft maximum at midlevels, while the upshear updraft maximum contains smaller contents of cloud liquid water (Fig. 2). The difference of maximum cloud liquid water in each updraft core is caused by lateral dynamic entrainment of elevated air parcels into the upshear updraft flank, in contrast to mainly surface-based parcels feeding the downshear updraft maximum (Chmielewski et al. 2020). As the storm intensifies with time, the greatest concentration of subsevere and severe hailstones progressively shifts toward the upshear updraft maximum (Figs. 4e,f–8e,f). The most favorable hail growth environment similarly shifts upshear with time, resulting in the larger hailstones later in the period (as supported by in situ surface observations). These larger hailstones are likely due to the ability to maintain the vertical velocity and terminal velocity quasi-balance within regions of stronger vertical velocities, thus having a longer residence time in the prime growth region.

With the larger masses and terminal velocities of the subsevere and severe hailstones, the horizontal winds are increasingly less capable of transporting these larger hailstones away from the updraft than the smaller melted particles. This process results in size sorting of hailstones within the storm—another factor in the highest concentrations of subsevere and severe hailstones residing increasingly near the updraft. Since the subsevere and severe hailstones are located near the updraft, they are embedded within the cyclonic flow on the southern side (right flank) of the updraft, which aids in the transport of the subsevere and severe hailstones around the mesocyclone (M88; Tessendorf et al. 2005). The highest concentrations of severe hailstones are found to the northeast of the downshear updraft maximum, where storm-relative horizontal cyclonic flow around the updraft deaccelerates due to convergence with the anticyclonic flow around the northern portion of the mesocyclone at midlevels in a region that will be referred to as the "downshear deceleration zone (DDZ)." The DDZ is
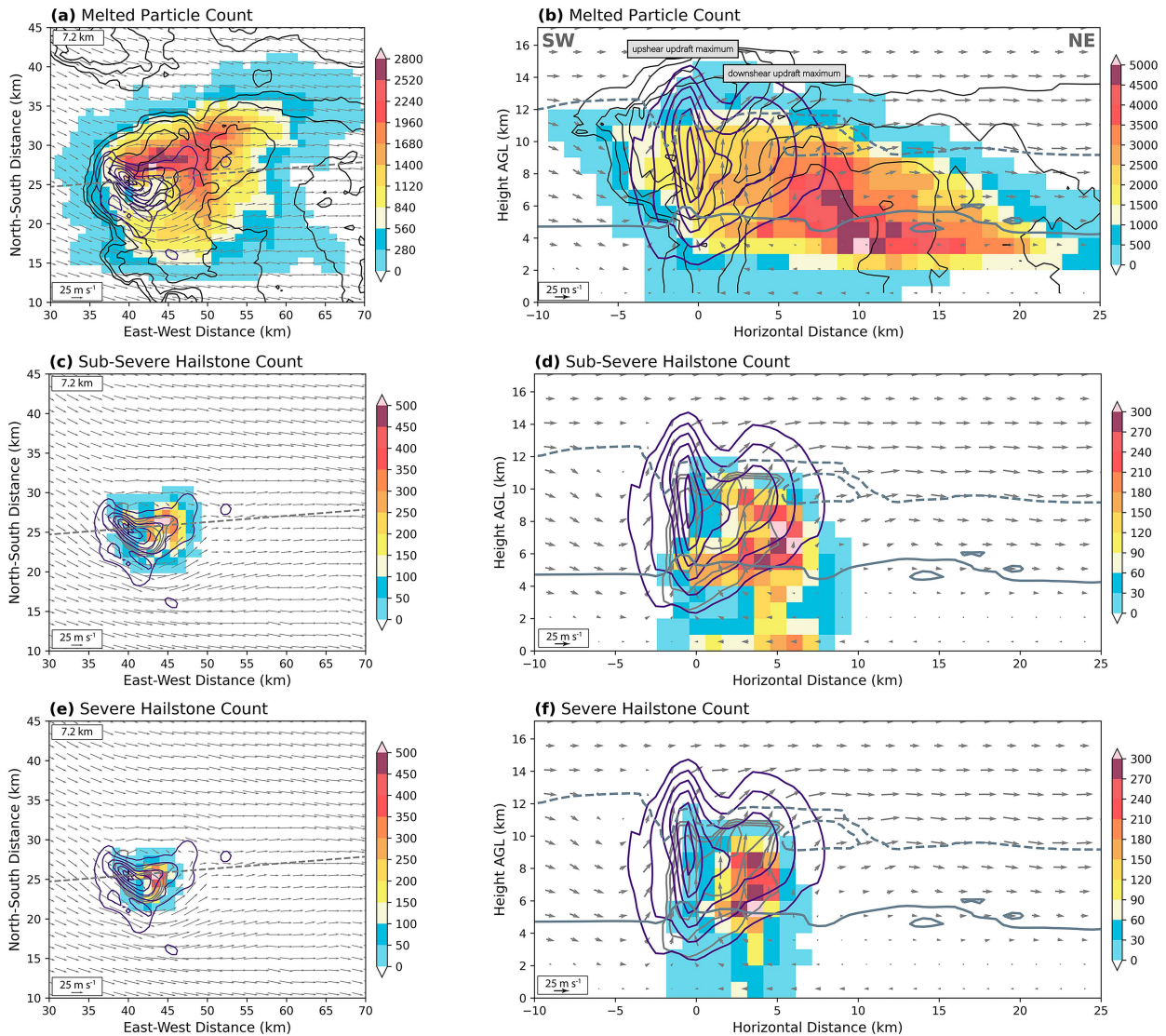
FIG. 6. As in Fig. 4, but at 2330 UTC.

located on the left (north) flank of the downshear updraft maximum, collocated with the upper-level mesocyclone center, as illustrated in Fig. 9 using the vertical and (minimal) horizontal air speeds. The minimal storm-relative flow that makes up the DDZ allows hailstones to reside longer in this region (Figs. 4e–8e) and continue to grow rather than be advected toward where there may be less supercooled cloud liquid water and where the vertical velocities may not be large enough to support the terminal velocities of large hailstones.

As the midlevel updraft (vertical velocities) decreases in spatial extent away from the updraft core, the collocated severe hail concentrations also decrease in spatial extent (Fig. 9) away from the updraft core, meaning that the DDZ is limited in space to where minimal storm-relative horizontal flow is located. Later in time (Figs. 9c,d) with increasing storm intensification, the DDZ expands spatially in the northwest (upshear) direction, supporting the largest hailstone concentration propagating

northwest (upshear) with time, thus furthering their ability to maintain a quasi-balance and increase residence time. The size of the DDZ is likely related to the vector orientation of storm-relative shear at midlevels (6–8 km) (hereinafter referred to as the "midlevel shear vector"), as the deacceleration (convergence) of midlevel horizontal flow on the left (northeast) flank of the updraft depends on the direction of the midlevel flow.

Differences in the updraft characteristics exist following the third updraft pulse at 2330 UTC (Fig. 4). A back-sheared anvil emerges after 2330 UTC (Figs. 6–8) as the main updraft volume and mass flux (Fig. 2a) persistently trend toward larger values. Some of the embryos that will subsequently grow to subsevere and severe hailstones are initialized west of the updraft by 2333 and 2339 UTC, respectively. A narrow corridor of hailstone embryos is present to the west of the updraft flank within the back-sheared anvil region from upper levels to slightly above the freezing level (Figs. 7d,f and 8d,f). These hailstone embryos
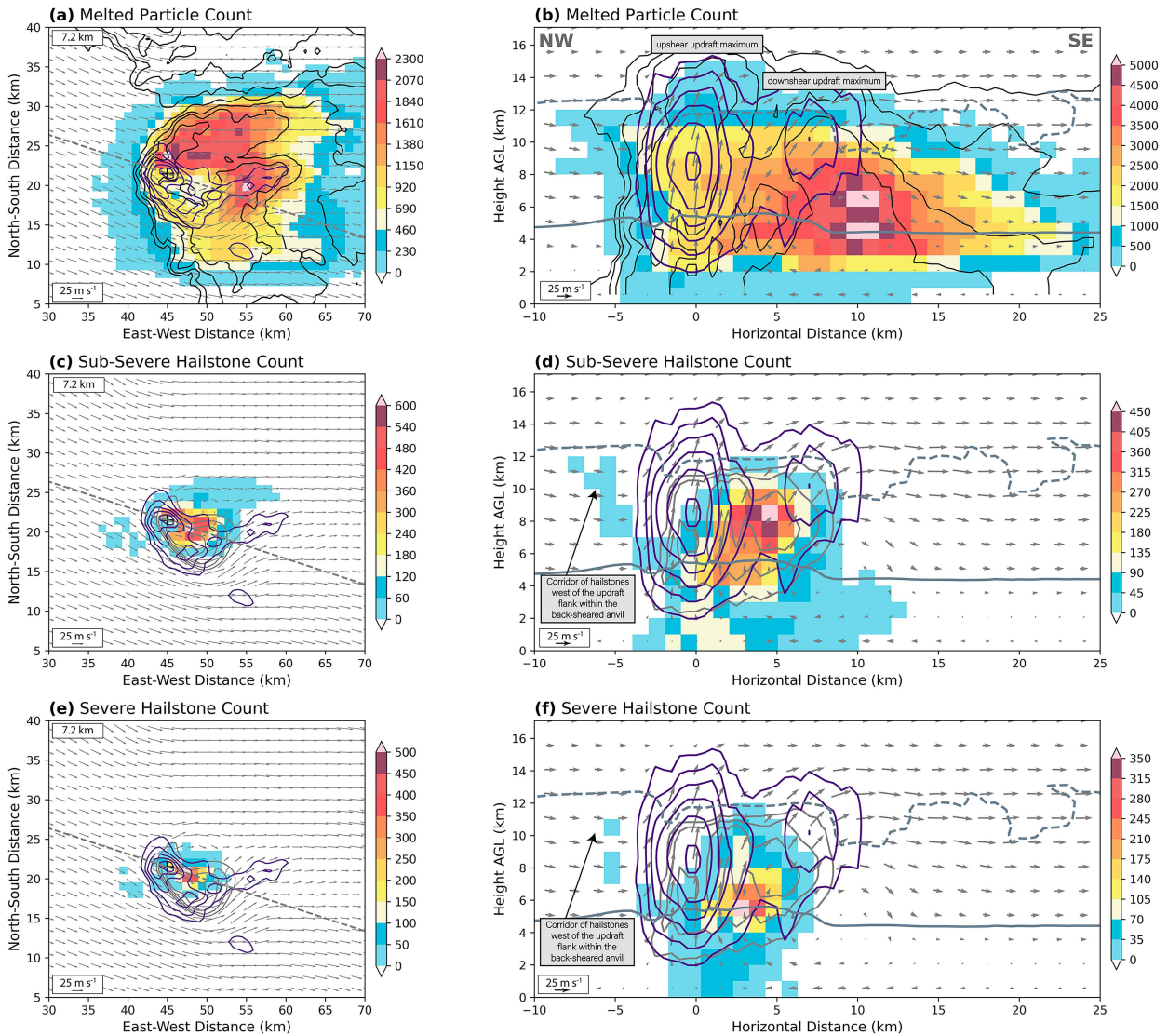
FIG. 7. As in Fig. 4, but at 2345 UTC.

initially descend within the back-sheared anvil in westerly midtropospheric flow and are subsequently ingested into the updraft region (Grant and van den Heever 2014). Reflectivity values locally exceeding 20–30 dBZ develop at subfreezing altitudes west of the updraft and beneath the back-sheared anvil, shown by Waugh et al. (2018), which strongly supports this graupel-embryo hailstone source region.

b. Hailstone residence time in updraft, supercooled cloud liquid, and ambient temperature

The time hailstones spend while growing (e.g., greater ice mass than the previous time step) within six defined subranges of vertical velocity, supercooled cloud liquid water, and ambient temperatures is compared among differing final diameter bins. Trajectories from all 24 analysis times resulting in a hailstone at the surface ≥ 1 cm are included, binned from 1 to 11 cm with 2-cm bin widths based on final diameter at the surface. We

seek to determine if relationships exist between final diameter at the surface and time spent while in the growth stage in a given vertical velocity, supercooled cloud liquid water, or ambient temperature range. Additionally, these results are used to expand the HGZ terminology.

As hailstone size at the surface increases in diameter, the time spent within vertical velocities in the range 0–10 m s^{-1} (Fig. 10a) decreases. There is no notable linear trend in the time spent within vertical velocities in the ranges of either 10–20 m s^{-1} (Fig. 10b) or 20–30 m s^{-1} (Fig. 10c). There is a positive linear trend within the first four final diameter bins for time spent within vertical velocities in the range 30–40 m s^{-1}, although the largest size bin (9–11 cm) is an outlier (Fig. 10c). This is likely a result of the terminal velocities of the largest hailstones being greater than 30–40 m s^{-1}, meaning that these hailstones must reside in regions of larger vertical velocities to remain aloft and continue to grow. An updraft containing at least 40 m s^{-1} would
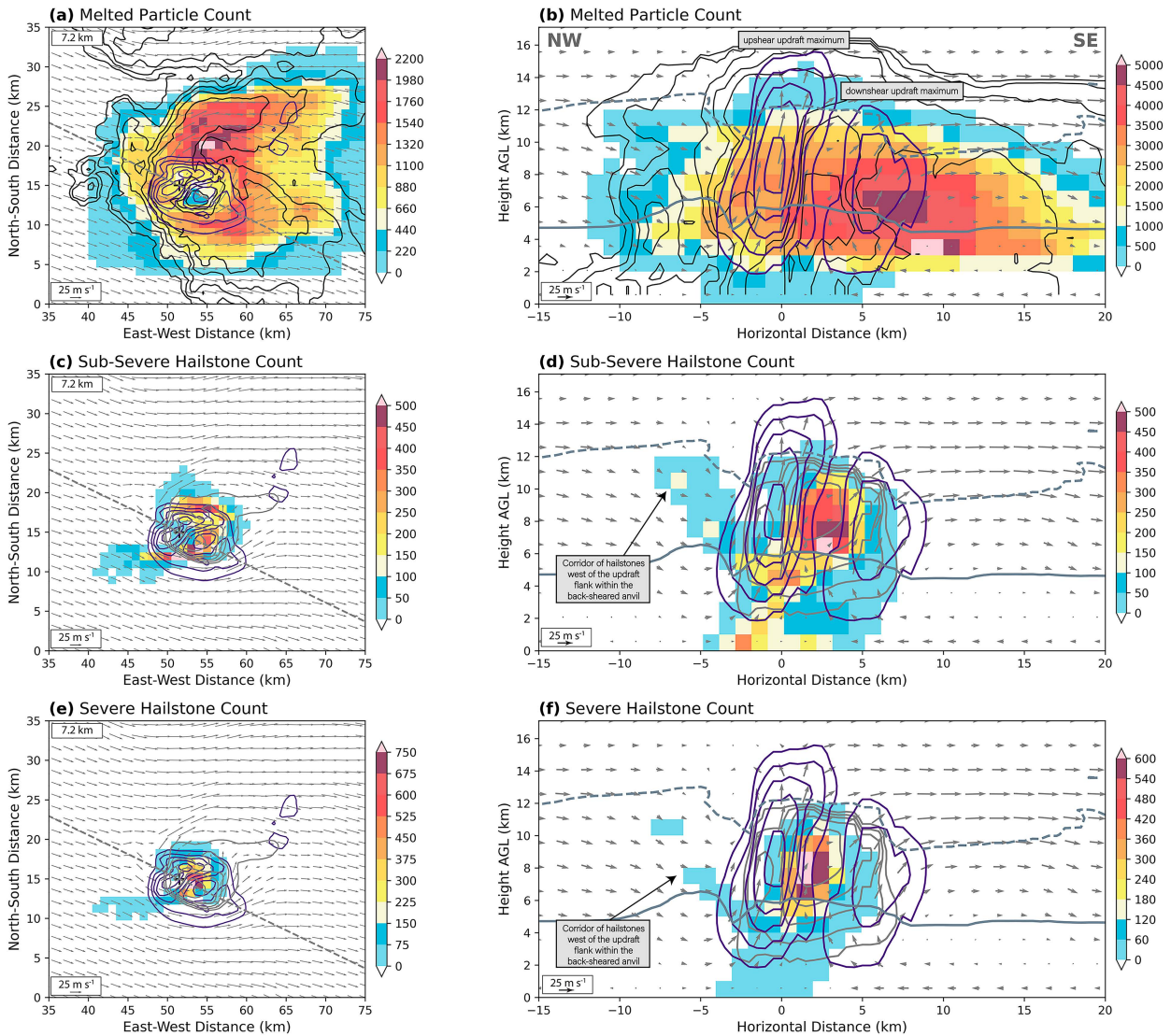
FIG. 8. As in Fig. 4, but at 0000 UTC.

support hail production of at least 1.0–3.0 cm, as most of the time spent growing is in vertical velocities < 40 m s^{-1}. The vertical velocities needed to produce large hail are more complex. Vertical velocities in the ranges of 40–50 m s^{-1} (Fig. 10d) and greater than 50 m s^{-1} (Fig. 4e) are sufficient to sustain a hailstone of 9–11 cm and exhibit a positive linear relationship between residence time in the given updraft range and hailstone diameter at the surface. This begs the question, if the stronger updraft results in larger hailstones, or if larger hailstones can combat the intense vertical velocities whereas smaller hailstones cannot?

To address the question, the absolute value of a hailstone's terminal velocity at every time step was subtracted from the vertical velocity at that point and the absolute value of the velocity difference was calculated, and the calculation is as follows: $|w - |v_t||$, shown in Fig. 11. These values are used to determine by how much the vertical velocities exceed the hailstone terminal velocities. It is found that most time spent in growth, for hailstones of

all sizes, is when the vertical velocity is <10 m s^{-1} greater than the hailstone's terminal velocity (Fig. 11a). Smaller amounts of time are spent when the vertical velocity is ≥10 and <20 m s^{-1} greater than the hailstone's terminal velocity (Fig. 11b) and near negligible amounts of time when the vertical velocity is ≥20 m s^{-1} greater than the hailstone's terminal velocity (Figs. 11c–f). For example, hailstones with a terminal velocity of ~70 m s^{-1} would require vertical velocities within approximately 10 m s^{-1} of that terminal velocity. This is likely why the greatest concentration of subsevere and severe hailstones shifts closer to the upshear updraft maximum with time. Defining an updraft supportive of hail growth as an updraft containing moderate velocities is not sufficient, as the production of large hailstones requires vertical velocities close to their growing terminal velocities over their entire life cycle.

The 1.0–3.0-cm hailstones spend the most time in supercooled cloud liquid water values in the range of 0–2 g kg^{-1}
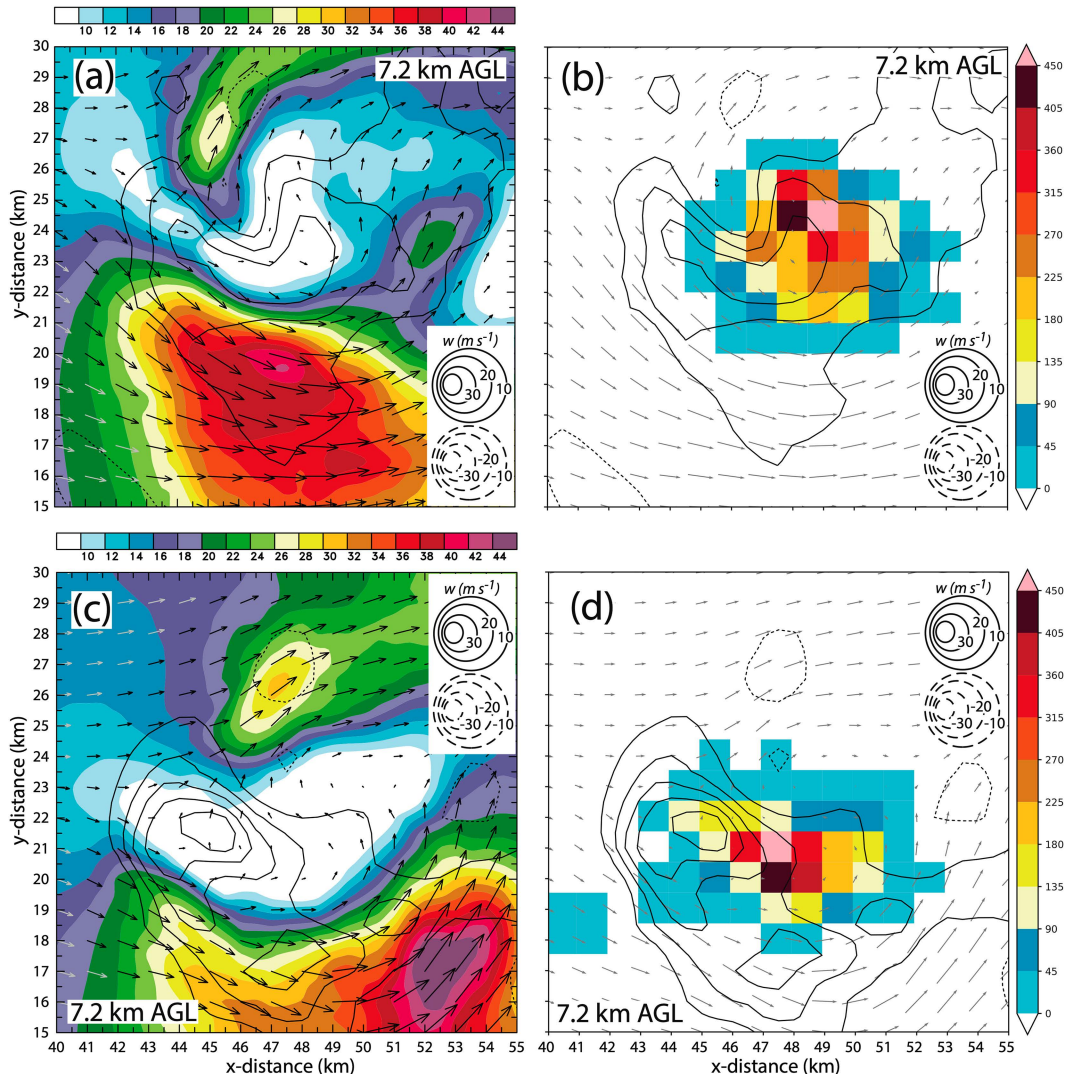
FIG. 9. Horizontal and vertical air speeds relative to severe hail concentrations at 7.2 km AGL at (a),(b) 2315 and (c),(d) 2345 UTC. (left) Horizontal wind speed (m s^{-1}) exceeding 10 m s^{-1} and (right) column-integrated severe hail concentration (as in Figs. 5e and 7e, respectively). Black contours (solid = positive, dotted = negative) are vertical velocity (m s^{-1}) with contour levels indicated by the inset. Vectors are storm-relative horizontal airflow, scaled by 1 km = 30 m s^{-1}.

(Fig. 12a). Time spent in 0–2 g kg^{-1} supercooled cloud liquid water values decreases as final diameter at the surface increases. The time spent in supercooled cloud liquid water values in the ranges of 2–4 g kg^{-1} (Fig. 12b) and 4–6 g kg^{-1} (Fig. 12c) shows no notable differences between any final diameter bins. However, supercooled cloud liquid water values in the ranges 6–8 g kg^{-1} (Fig. 12d) and 8–10 g kg^{-1} (Fig. 12e) exhibit a positive linear relationship between time spent in higher supercooled cloud liquid water and final hailstone diameter at the surface. For those thresholds, as hailstone diameter at the surface increases, the residence time in the latter supercooled cloud liquid water ranges also increases. The absence of the linear trend for supercooled water contents exceeding 10 g kg^{-1} (Fig. 12f) is likely due to the limited number of hailstones that encounter supercooled water contents

of such high cloud mixing ratios. In contrast to the vertical velocity threshold results, there does not appear to be a limiting threshold value above which there is too much supercooled water. Tessendorf et al. (2005) stated that embryo-sized particles enter the updraft, and they can "achieve hail sizes and fallout before passing through the layer of high cloud liquid water." Their statement indicates that much growth can occur in values or lower supercooled cloud liquid water, in agreeance with the results there that any amount of supercooled cloud liquid water can be sufficient for growth, as hailstones of all sizes do spend time growing in lower supercooled cloud liquid water.

The larger hailstones spend more time during the growth phase at warmer ambient (environmental) temperatures, specifically ambient temperatures of ≥−10° and <−20°C (Figs. 13b,c),
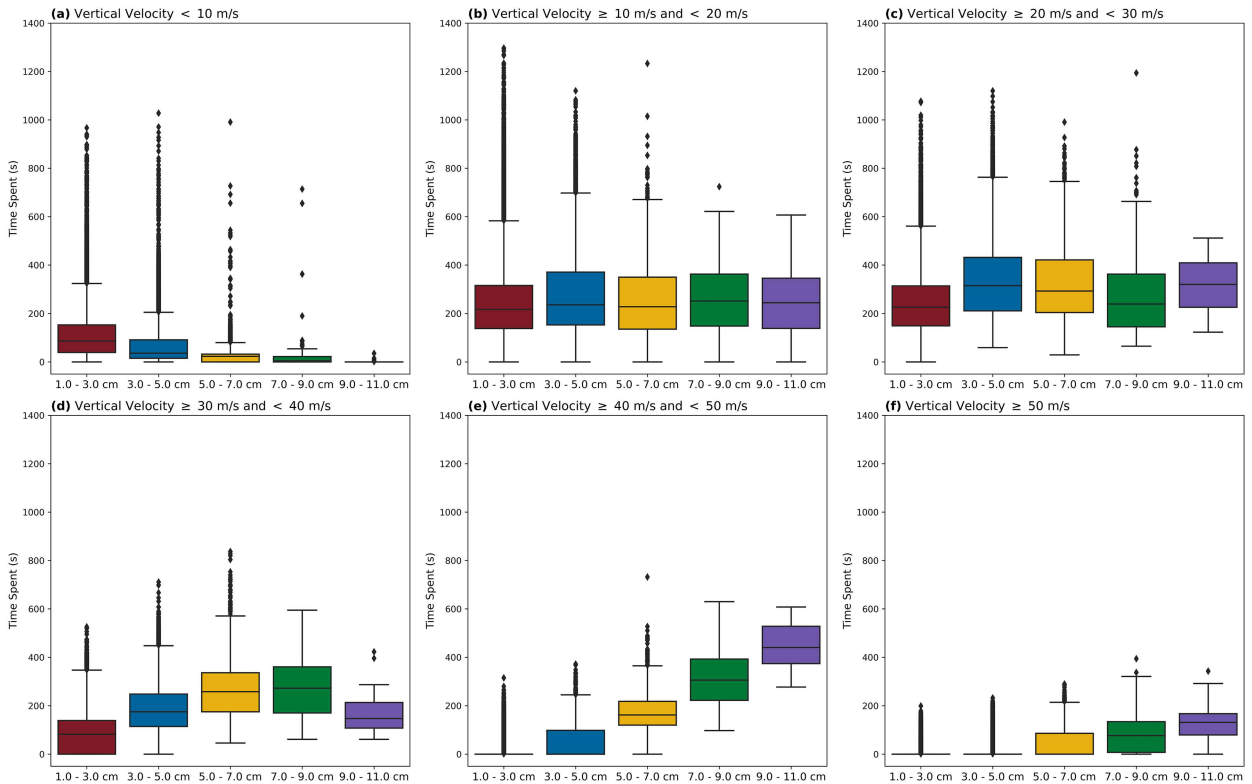
FIG. 10. Time (s) hailstones spend during growth within a given range of vertical velocity values as a function of final hailstone size at the ground for (a) ≥0 and <10 m s^{-1}, (b) ≥10 and <20 m s^{-1}, (c) ≥20 and <30 m s^{-1}, (d) ≥30 and <40 m s^{-1}, (e) ≥40 and <50 m s^{-1}, and (f) ≥50 m s^{-1}. Hailstones from 2251 to 0000 UTC are included if their final diameter at the surface was at least 1 cm. Five different size bins of D_{eq} at the surface are used: 1–2 cm (red), 2–3 cm (blue), 3–4 cm (yellow), 4–5 cm (green), and 5–6 cm (purple). The color-filled area denotes the interquartile range, or the points between the first quartile (upper) and third quartile (lower) of the data. The black line within the color fill is the median of the data. The whiskers represent 1.5× the interquartile range. Solid diamonds represent outliers, or points that reside outside of the whiskers.

than the smaller hailstones. Typically, the HGZ is defined as temperatures between −10° and −40°C, although in our study, most growth occurs between ambient temperatures of ≥−10° and <−30°C (Figs. 13b–d). At ambient temperatures of ≥−10° and <0°C (Fig. 13b) and ≥−20° and <−10°C (Fig. 13c), there is a general positive linear trend as final hail diameter at the surface increases, time spent in those ambient temperatures increases. This is not all that surprising, as wet growth typically occurs at warmer temperatures, and large hailstones spend the most time, especially at the end of their life cycle in wet growth (Knight and Knight 2005). Additionally, Tessendorf et al. (2005) found the maxima in hail echo volume to be between −10°C and the melting level. The same trend does not hold for colder ambient temperatures of ≥−30° and <−20°C (Fig. 12d), ≥−40° and <−30°C (Fig. 13e), or ≥−40°C (Fig. 13f). This is likely a result of the larger hailstone trajectories remaining at lower heights in the storm, where warmer temperatures are found and smaller hailstones take trajectory pathways at higher heights within the storm. While hailstones do not spend time in growth when ambient temperatures are ≥0°C (Fig. 11a), there is melting occurring at these temperatures. Quantification of melting is beyond the scope of this study, but trajectories computed using ASZ16-HAILCAST

do contain melting information and could be an important avenue of future work.

In combining these results with the definition of the HGZ, we can extend the definition of the HGZ to be a region of the storm consisting of 1) any vertical velocities ≥ 10 m s^{-1}, 2) any nonzero amount of supercooled cloud liquid water, and 3) ambient temperatures between 0° and −40°C. This region hereafter will be referred to as the "prime growth region," as these results and past literature highlighted in previous sections have shown that temperatures, supercooled water, and updraft speeds are all needed in conjunction to support hail growth. These values provide a wide range, but hailstones spend a nonnegligible amount of time growing in conditions within these ranges and therefore are included in our definition of the prime growth region. The most ideal values for a given hailstone at a given time vary, but the region defined here is all encompassing of small to large hail production.

c. Trajectories of largest hailstones relative to storm morphology

The trajectory paths of a small sample of the largest hailstones with respect to horizontal airflow, vertical velocity, reflectivity,
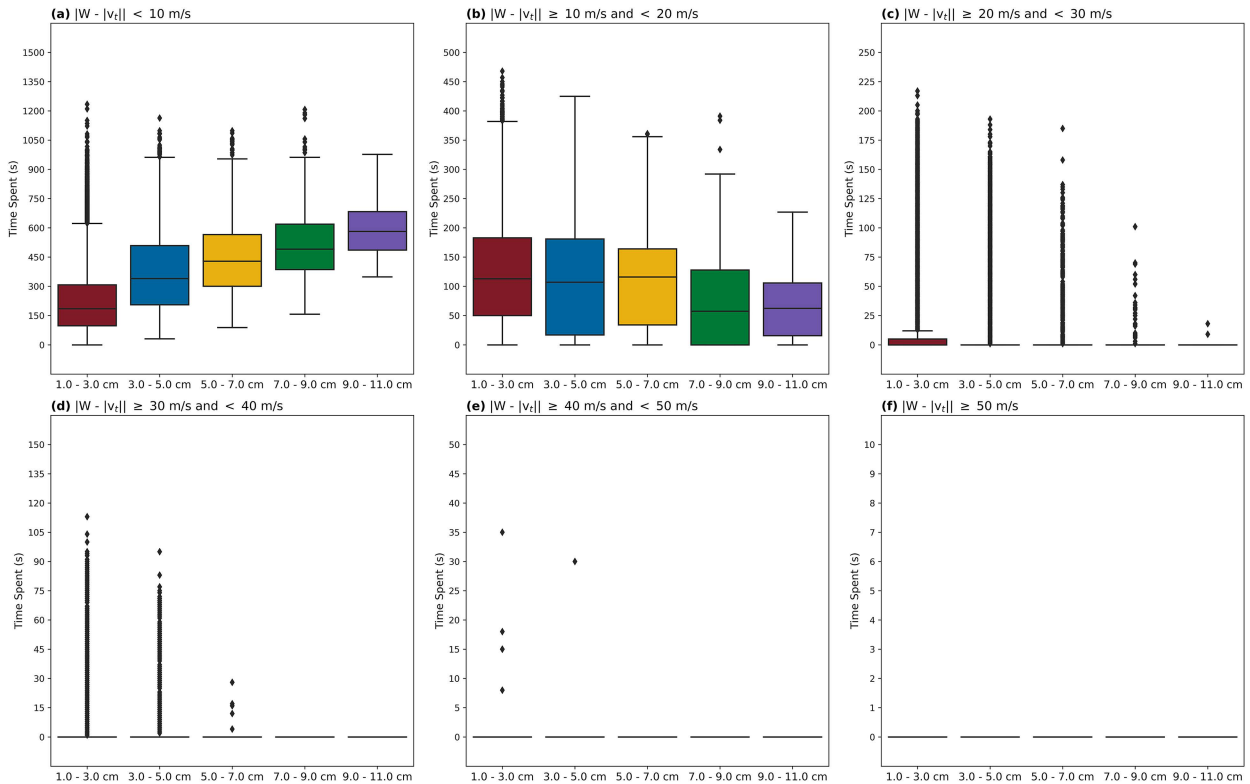
FIG. 11. Time (s) hailstones spend during growth within a given range of vertical velocity and terminal velocity differences given by $|w - |v_t||$, as a function of final hailstone size at the ground for (a) ≥ 0 and <10 m s^{-1}, (b) ≥ 10 and <20 m s^{-1}, (c) ≥ 20 and <30 m s^{-1}, (d) ≥ 30 and <40 m s^{-1}, (e) ≥ 40 and <50 m s^{-1}, and (f) ≥ 50 m s^{-1}. Hailstones from 2251 to 0000 UTC are included if their final diameter at the surface was at least 1 cm. Five different size bins of D_{eq} at the surface are used: 1–2 cm (red), 2–3 cm (blue), 3–4 cm (yellow), 4–5 cm (green), and 5–6 cm (purple). The color-filled area denotes the interquartile range, or the points between the first quartile (upper) and third quartile (lower) of the data. The black line within the color fill is the median of the data. The whiskers represent 1.5× the interquartile range. Solid diamonds represent outliers, or points that reside outside of the whiskers. Note the difference in y axis for each panel.

and supercooled cloud liquid water during early and late time periods broadly illustrate the evolving storm characteristics associated with some of the largest hail. The predominant trajectories of the 10 largest hailstones initialized at 2321 UTC ("downshear group"), ranging from 6.84 to 8.38 cm in final diameter, are sourced around the main updraft and represent the early-middle period of large hail growth (Figs. 14 and 15). As an additional example, 10 severe hail trajectories ranging from 2.55 to 6.41 cm are shown from the 2339 UTC initialization time ("upshear group") that are sourced within the storm's back-sheared anvil beyond the upshear updraft flank (Figs. 16 and 17).

Between initialization (2321 UTC) and ~2327 UTC, the downshear-grouped hailstones are advected counterclockwise around the mesocyclone along the BWER edge and high reflectivity gradient in the storm-relative reference frame (Figs. 14a–c and 15a–c). The midlevel storm-relative flow diverges around the updraft on the upshear side and reconverges on the downshear side, resulting in deacceleration of the flow, thus the creation of the DDZ. Between 2327 and 2333 UTC (Figs. 14c–e), the hailstones move upshear through the northern mesocyclonic flank toward the upshear updraft core, where the strong midlevel horizontal flow advecting the hailstones has lessened through the

previously defined DDZ. Since the updraft dominates horizontal flow at higher levels of the DDZ (Figs. 14c–e and 15c–e), the hailstones ascend to the upper end of the midlevels (7–9 km). By 2336 UTC, there is a variation in the horizontal (Fig. 14f) and vertical (Fig. 15f) positions of the hailstones. Hailstones that encounter higher supercooled liquid water prior to this point are likely to gain more mass and therefore have larger terminal velocities and require larger updrafts to remain aloft. With differing masses between the 10 hailstones, the trajectories continue to diverge for the remainder of the period. However, the hailstones remain within the DDZ throughout the remainder of their growth phase. After 2339 UTC (Figs. 14g–i and 15g–i), the hailstones begin their final descent to ground. The hailstones fall to the surface along the gradient of the BWER and high reflectivity core and below the midlevel updraft maximum.

Why do these trajectories produce among the largest hailstones at the surface? As described previously, the DDZ provides an area of relatively weak, mesocyclonic horizontal flow on the left flank of the downshear updraft core. The DDZ provides area where hailstones can remain aloft at a relatively constant height without being transported away from the prime growth region. The DDZ is a feature seen in the Kingfisher,
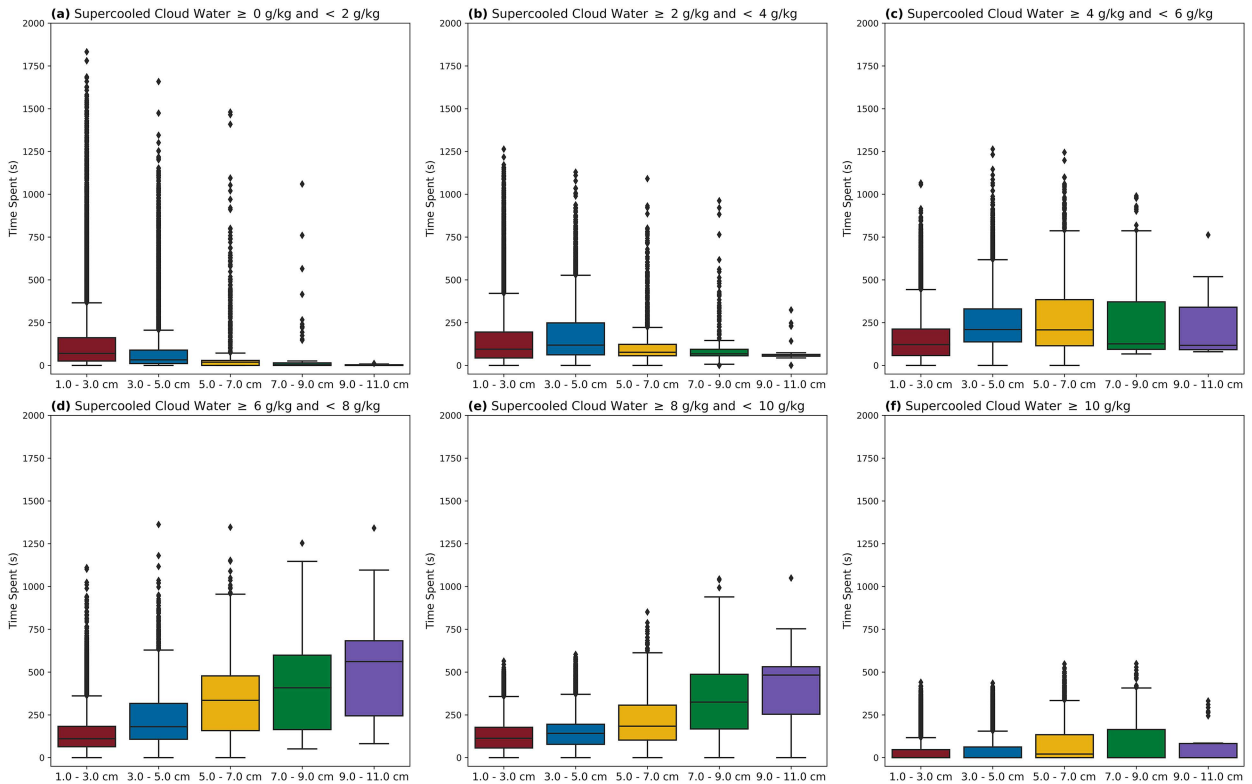
FIG. 12. Time (s) hailstones spend during growth within a given range of supercooled cloud liquid water values as a function of final hail-stone size at the ground for (a) ≥0 and <2 g kg^{-1}, (b) ≥2 and <4 g kg^{-1}, (c) ≥4 and <6 g kg^{-1}, (d) ≥6 and <8 g kg^{-1}, (e) ≥8 and <10 g kg^{-1}, and (f) ≥10 g kg^{-1}. Hailstones from 2251 to 0000 UTC are included if their final diameter at the surface was at least 1 cm. Five different size bins of D_{eq} at the surface are used: 1–2 cm (red), 2–3 cm (blue), 3–4 cm (yellow), 4–5 cm (green), and 5–6 cm (purple). The color-filled area denotes the interquartile range, or the points between the first quartile (upper) and third quartile (lower) of the data. The black line within the color fill is the median of the data. The whiskers represent 1.5× the interquartile range. Solid diamonds represent outliers, or points that reside outside of the whiskers.

Oklahoma, supercell, and we hypothesize a common feature of large hail-producing supercells. Previous studies hinted at this paradigm, proposing that the initially weak horizontal flow within the main updraft edge with hailstones that have already developed increased mass and fall speed could subsequently increase the residence time by extending the quasi-balance between the updraft and terminal velocities (Rasmussen and Heymsfield 1987b; Heymsfield 1983; Foote 1984) and thus produce larger hail. Kumjian et al. (2021) noted differences in midlevel storm structure between large and small hail times, specifically, differences in storm-relative flow on the northwest side of the updraft, which is where the DDZ would be located.

After the back-sheared anvil develops, an additional source region for severe hailstones (as seen in the Browning and Foote 1976 conceptual model) results in another severe hailstone trajectory pathway by 2339 UTC. These upshear trajectories range from 2.55 to 6.41 cm in diameter at the surface with a mean final diameter of 3.68 and a median of 3.20 cm. The total residence time ranges from 1415 to 1989 s with a mean total residence time of 1583.8 and a median of 1507 s. These upshear-grouped trajectories (Figs. 16 and 17) initiate within and subsequently descend following the ambient winds through the lower levels of the

back-sheared anvil (Figs. 16a and 17a) where reflectivities larger than 20 dBZ are plausibly associated with small graupel embryos (e.g., section 3i). The embryos subsequently reach the upshear updraft flank by 2348 UTC after roughly 12 min into their life cycle (Figs. 16a–d and 17a–d). By 2351 UTC, the growing hailstones have ascended into the midlevel cloud water mixing ratio core on the southwestern edge of the mesocyclone (Figs. 16e and 17e). Similarly to the early stages of the downshear group after 2321 UTC, the upshear trajectories are subsequently advected counterclockwise through the mesocyclone. As with the downshear group, the upshear-grouped hailstones are subsequently lofted by 2354 UTC as updrafts greatly exceed the horizontal flow around the mesocyclone (Figs. 16f and 17f). The upshear trajectories ascend much higher (up to ~11 km) than the downshear group, due to lesser mass and smaller hailstone terminal velocities relative to the strong updrafts. Since the upshear group is lofted higher, they reach the upper levels of the storm where increasing horizontal flow advects them farther downshear from the updraft core. Foote (1984) noted a similar finding, observing that hailstones with less initial growth were lofted higher in the storm in comparison with hailstones with greater growth before reaching the strong updraft region.
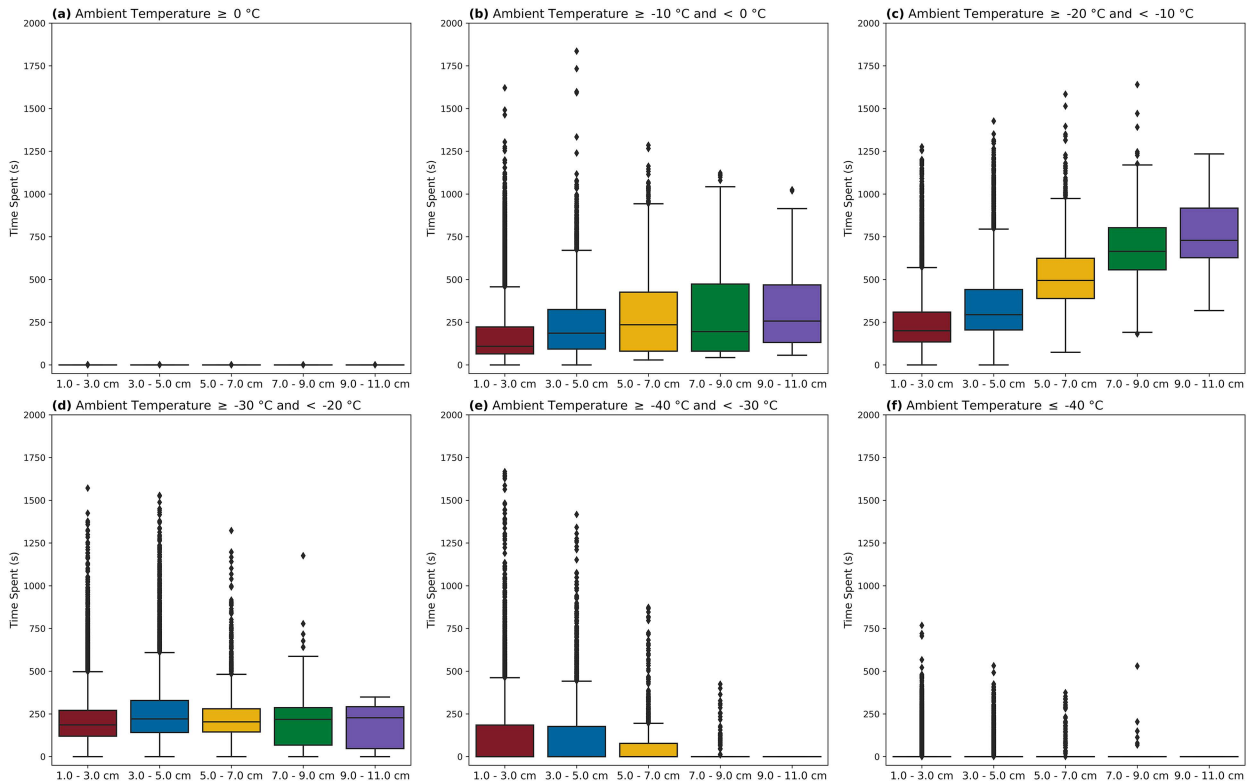
FIG. 13. Time (s) hailstones spend during growth within a given range of ambient temperature values as a function of final hailstone size at the ground for (a) ≥0°C, (b) ≥−10° and <0°C, (c) ≥−20° and <−10°C, (d) ≥−30° and <−20°C, (e) ≥−40° and <−30°C, and (f) ≤−40°C. Hailstones from 2251 to 0000 UTC are included if their final diameter at the surface was at least 1 cm. Five different size bins of D_{eq} at the surface are used: 1–2 cm (red), 2–3 cm (blue), 3–4 cm (yellow), 4–5 cm (green), and 5–6 cm (purple). The color-filled area denotes the interquartile range, or the points between the first quartile (upper) and third quartile (lower) of the data. The black line within the color fill is the median of the data. The whiskers represent 1.5× the interquartile range. Solid diamonds represent outliers, or points that reside outside of the whiskers.

These limited numbers of the largest hailstone trajectories, which do not represent the only pathways large hailstones can take, are used to conceptualize the predominant large-hail trajectory pathways in relation to the updraft, supercooled cloud liquid water, and precipitation fields in the Kingfisher supercell. The following result section employs a much larger ensemble of trajectories to more broadly analyze additional pathways resulting in large surface hailstones.

5. Results: Organization of large hail growth as illustrated by trajectory clusters

The subset of all trajectories that produced hailstones exceeding 4.5 cm in diameter at the surface ($n = 3281$) were processed by a clustering algorithm (Adams-Selin 2023), yielding useful subgroupings of common trajectory pathways to help evaluate the differences and similarities of trajectories relative to the storm motion. In brief, the computationally intensive clustering algorithm operates on hail trajectories following their conversion to an updraft-relative reference frame. Individual hail trajectories are first partitioned into line segments, which are clustered into groups using a modified Density-Based Spatial

Clustering of Applications with Noise (DBSCAN; Ester et al. 1996; Schubert et al. 2017) with a custom distance matrix calculation following the method of Lee et al. (2007). The distance between trajectory segments is determined via both Euclidean distance in multiple dimensions and segment alignment, so segments must be both close in space and follow parallel paths to be grouped. Once the cluster memberships of all the partitions are determined, the parent trajectories are examined. If a group of parent trajectories share at least two partition cluster memberships in common, that group is termed a "parent cluster." A subjective review of parent clusters will then combine those with broadly similar trajectory profiles into "superclusters," for ease of figure display. The interested reader is referred to Adams-Selin (2023) for more details. The overall objective of supercluster identification is to identify predominant, highly populated hail trajectory groupings to better generalize results for improved process understanding of hail growth (particularly for severe and giant hail).

A total of 13 resultant "superclusters" of trajectory pathways (denoted in the range A–N) were identified for further analysis. While a detailed summary description of every supercluster is beyond the scope of this study, selected clusters are shown to
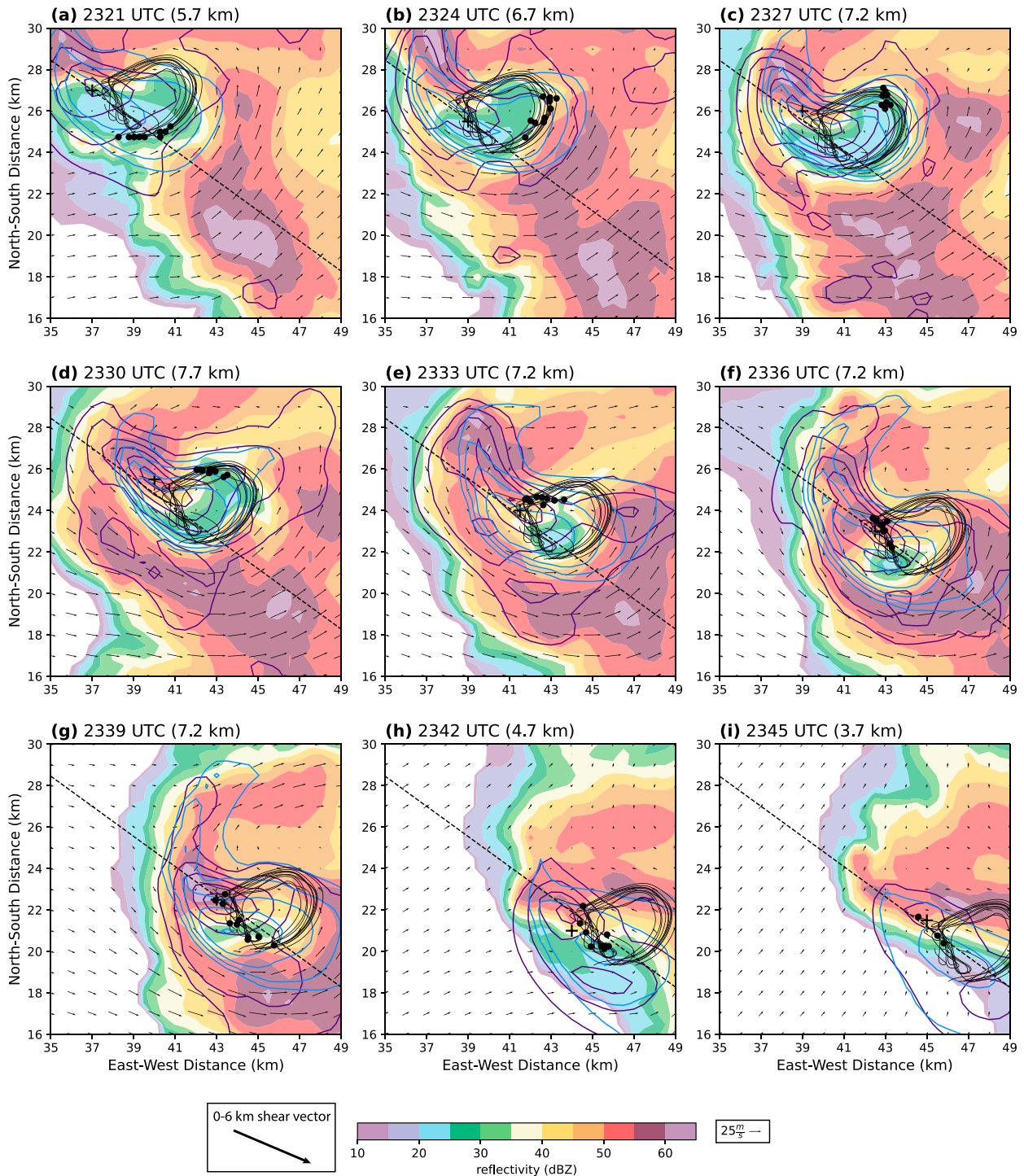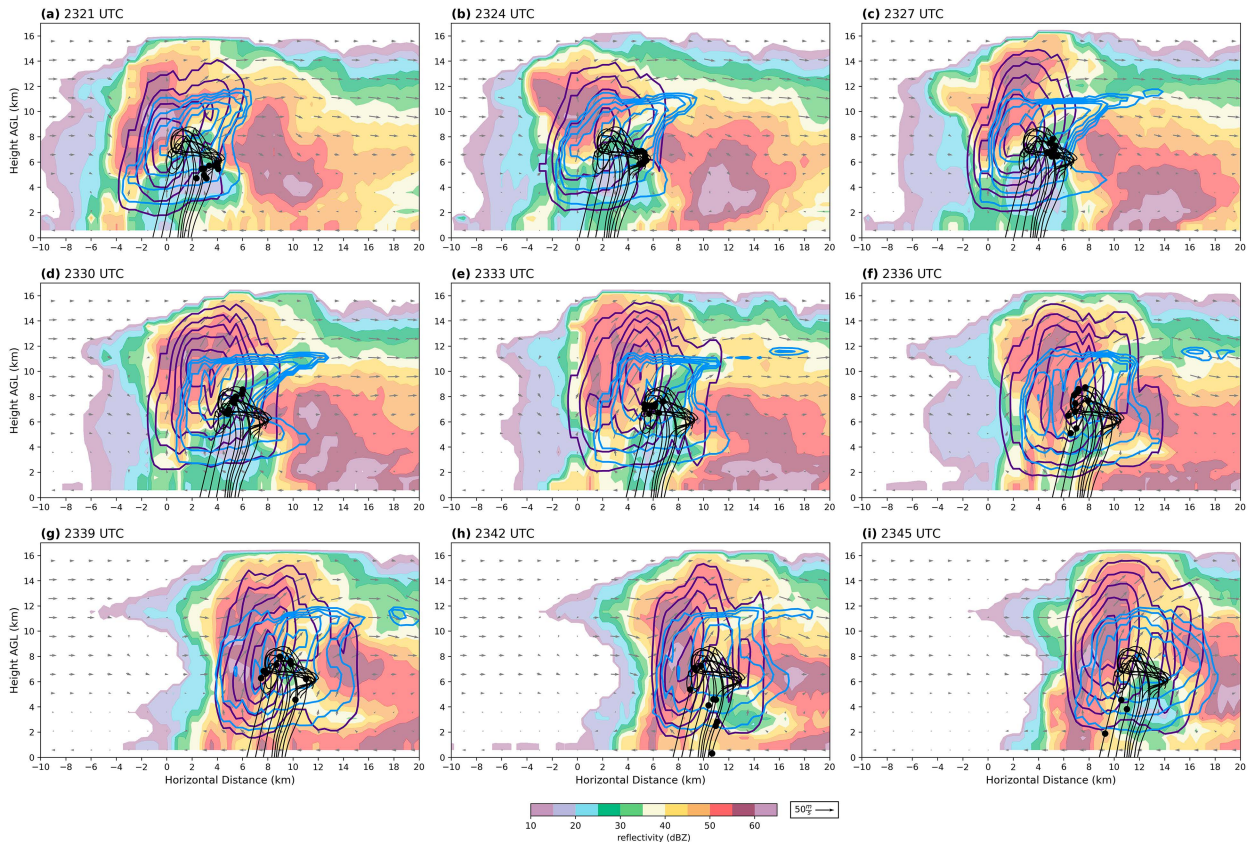
FIG. 14. Horizontal projections of the 10 largest trajectories (black lines) initialized at 2321 UTC. Reflectivity (color fill, starting at 20 dBZ at 10-dBZ intervals), vertical velocity (purple contours, starting at 10 m s^{-1} at 10 m s^{-1} intervals), and cloud water mixing ratio (blue contours, starting at 2 g kg^{-1} at 2 g kg^{-1} intervals) are shown from initialization (2321 UTC) through the last time period where any of the 10 trajectories are still valid (2345 UTC) at 7.2 km. Wind vectors denoted by the gray arrows are storm-relative also at 7.2 km. The black "+" denotes the midlevel updraft center at each time step. The black dots denote where along the trajectory the hailstone is at (a) 2331, (b) 2324, (c) 2327, (d) 2330, (e) 2333, (f) 2336, (g) 2339, (h) 2342, and (i) 2345 UTC. A black "x" is shown where the maximum of the mean vertical velocity at all levels is found in (a). The cross section cuts through this point in (a) and remains the same in (a)–(i). The long, heavy black arrow at bottom denotes the orientation of the 0-6-km shear vector, while the magnitude of this vector is shown in Fig. 2.

FIG. 15. Vertical cross-sectional projections of the 10 largest trajectories (black lines) initialized at 2321 UTC. Reflectivity (color fill, starting at 20 dBZ at 10-dBZ intervals), vertical velocity (purple contours, starting at 10 m s^{-1} at 10 m s^{-1} intervals), and cloud water mixing ratio (blue contours, starting at 2 g kg^{-1} at 2 g kg^{-1} intervals), and storm-relative wind vectors (gray arrows) are shown from initialization (2321 UTC) through the last time period where any of the 10 trajectories are still valid (2345 UTC) in a cross section denoted in Fig. 11. The black dots denote where along the trajectory the hailstone is at (a) 2331, (b) 2324, (c) 2327, (d) 2330, (e) 2333, (f) 2336, (g) 2339, (h) 2342, and (i) 2345 UTC.

exemplify how results from section 4 are reflected in the more robustly expanded super-clustered trajectory groupings. To differentiate the range of growth processes within the selected superclusters, ambient hail-environmental variables (Figs. 18a–d) and hailstone growth characteristics (Figs. 18e–h) are statistically compared. The number of trajectories included in each supercluster over time is shown in Fig. 19. The average and varying-footprint storm-relative trajectory paths, or "representative trajectory" of each of the four clusters, are shown by thick solid lines, while paths of all individuals are shown by thinner lines with dots to indicate the starting position and arrows to indicate the ending position in Fig. 20. Note that the representative trajectory is less accurately depicted in the early portion of the trajectory when the embryo source positions vary greatly among the individual trajectories within the supercluster, a matter to be addressed in future work.

a. Supercluster A

Supercluster A, which contains 279 trajectories (Fig. 20a), is the predominant pathway for hailstones ≥ 4.5 cm in this dataset. It is primarily distinguished from the other superclusters

during the first ~10–15 min of evolution (i.e., between ~33 and 25 min prior to reaching the surface). Although the 10 upshear-initialized hailstones from within the back-sheared anvil (e.g., Figs. 16 and 17, section 4b) have a mean maximum diameter at ground less than 4.5 cm, their overall characteristics after their first ~5–10 min during updraft injection are broadly consistent with supercluster A (Fig. 18). Supercluster A begins within rather weak updraft speeds (Fig. 18a) and low cloud liquid water (Fig. 18d), as expected for a hailstone initialized upshear from the prime growth region. Cloud liquid water subsequently increases gradually until ~5 min before reaching the surface when they begin their final descent. Between ~15 and 10 min prior to reaching the surface, the updraft speeds (Fig. 18a) and cloud liquid water (Fig. 18d) increase more rapidly while the cloud temperatures decrease (Fig. 18b), resulting in the hailstones growing (Figs. 18e–g) and achieving solid-ice density (Fig. 18h).

These Lagrangian variables following supercluster A imply that these hailstones began in a less favorable environment and gradually moved toward an environment supportive of large hail growth. The representative trajectory of supercluster A begins to
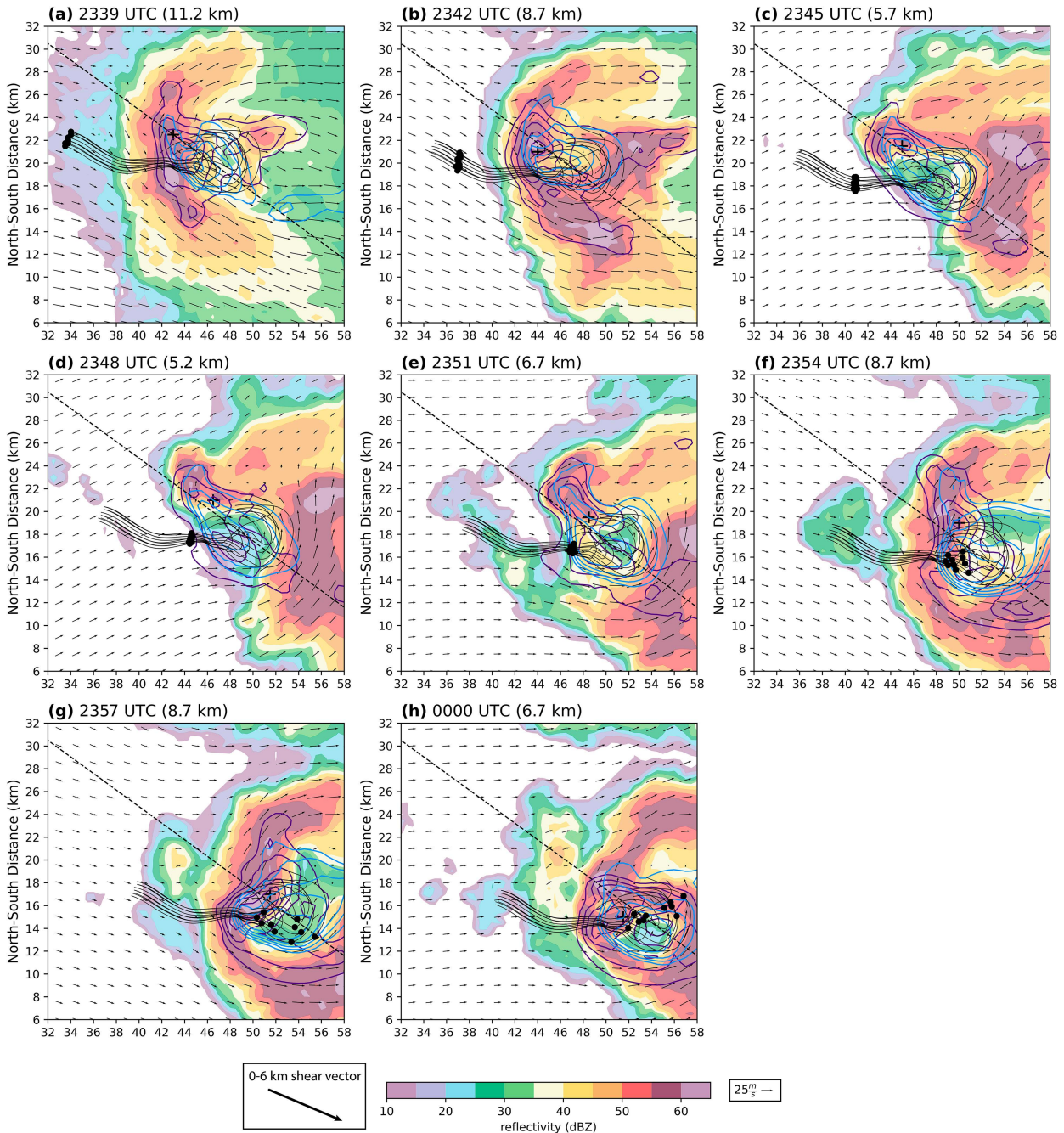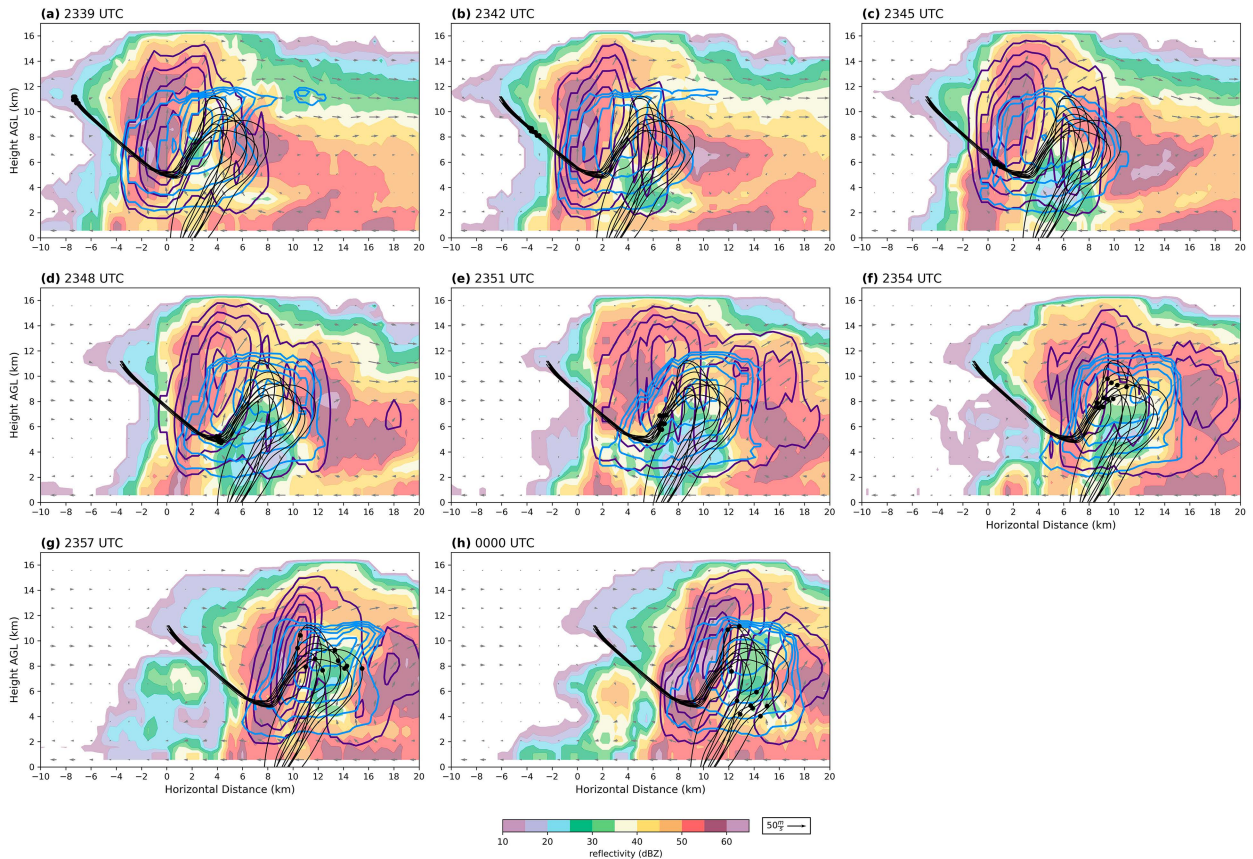
FIG. 16. Horizontal projections of the 10 largest-hail trajectories (black lines) initialized upshear of the updraft and the 11 largest-hail trajectories initialized from the upshear source region at 2339 UTC. Reflectivity (color fill, starting at 20 dBZ at 10-dBZ intervals), vertical velocity (purple contours, starting at 10 m s^{-1} at 10 m s^{-1} intervals), and cloud water mixing ratio (blue contours, starting at 2 g kg^{-1} at 2 g kg^{-1} intervals) are shown from initialization (2339 UTC) through the last time period available (0000 UTC) at 7.2 km. Wind vectors denoted by the gray arrows are storm-relative also at 7.2 km. The black "+" denotes the midlevel updraft center at each time step. The black dots denote where along the trajectory the hailstone is at (a) 2339, (b) 2342, (c) 2345, (d) 2348 (e) 2351, (f) 2354, (g) 2357, and (h) 0000 UTC. A black "x" is shown where the maximum of the mean vertical velocity at all levels is found in (a). The cross section cuts through this point in (a) and remains the same in (a)–(h).

FIG. 17. Vertical cross-sectional projections of the 10 largest-hail trajectories (black lines) initialized upshear of the updraft and the 11 largest-hail trajectories initialized from the upshear source region at 2339 UTC. Reflectivity (color fill, starting at 20 dBZ at 10-dBZ intervals), vertical velocity (purple contours, starting at 10 m s^{-1} at 10 m s^{-1} intervals), and cloud water mixing ratio (blue contours, starting at 2 g kg^{-1} at 2 g kg^{-1} intervals), and storm-relative wind vectors (gray arrows) are shown from initialization (2339 UTC) through the last time period where any of the 10 trajectories are still valid (2345 UTC) in a cross section denoted in Fig. 13. The black and brown dots denote where along the respective trajectory the hailstone is at (a) 2339, (b) 2342, (c) 2345, (d) 2348, (e) 2351, (f) 2354, (g) 2357, and (h) 0000 UTC.

the northeast of the updraft maximum, initiating a wide counterclockwise loop through the mesocyclone around the updraft where the greatest mass growth rate occurs (Figs. 18f and 20). The largest hailstones are found within this cyclonic flow around the updraft on its southern flank. These results are consistent with Z83 and Foote (1984) who found hailstone trajectories that began on the southwest side of the main updraft were transported cyclonically around the updraft periphery within the midlevel mesocyclone. Since supercluster A is lofted to the upper fringes of the midlevels and thus experiences increased horizontal flow with height, supercluster A is advected further downshear (Fig. 20) and has the greatest leftward displacement relative to storm motion of any cluster.

b. Supercluster N

Although supercluster N is similar to supercluster A (albeit with a residence time of ~8 min less than supercluster A), supercluster N nevertheless achieves greater average mass (Fig. 18g) and diameter (Fig. 18e). The overall characteristics of the 10 hailstone trajectories initialized in the downshear updraft core and mesocyclone (e.g., Figs. 14 and 15, section 4a) are broadly consistent with both supercluster N and supercluster A within ~25 min before reaching the surface (Fig. 18). A smaller cyclonic loop is made by supercluster N (Fig. 20d) than by supercluster A (Fig. 20a), although similar positioning relative to the updraft core is associated with very similar peak supercooled cloud liquid water (Fig. 18d). However, supercluster N travels through warmer and higher supercooled cloud liquid water contents for the first ~15 min, allowing greater growth. The 50th percentile peak in the mass growth rate of supercluster N between ~10 and 5 min before reaching the surface exceeds the 75th percentile of any other supercluster at that point in time. The significantly larger mass growth rate might be attributed to more efficient collection of cloud liquid water near the updraft center, resulting in a shorter residence time. Although other superclusters have broadly similar characteristics to superclusters A and N (e.g., superclusters D, E, and F; not shown), they also have various nuanced differences that objectively distinguish their pathways.
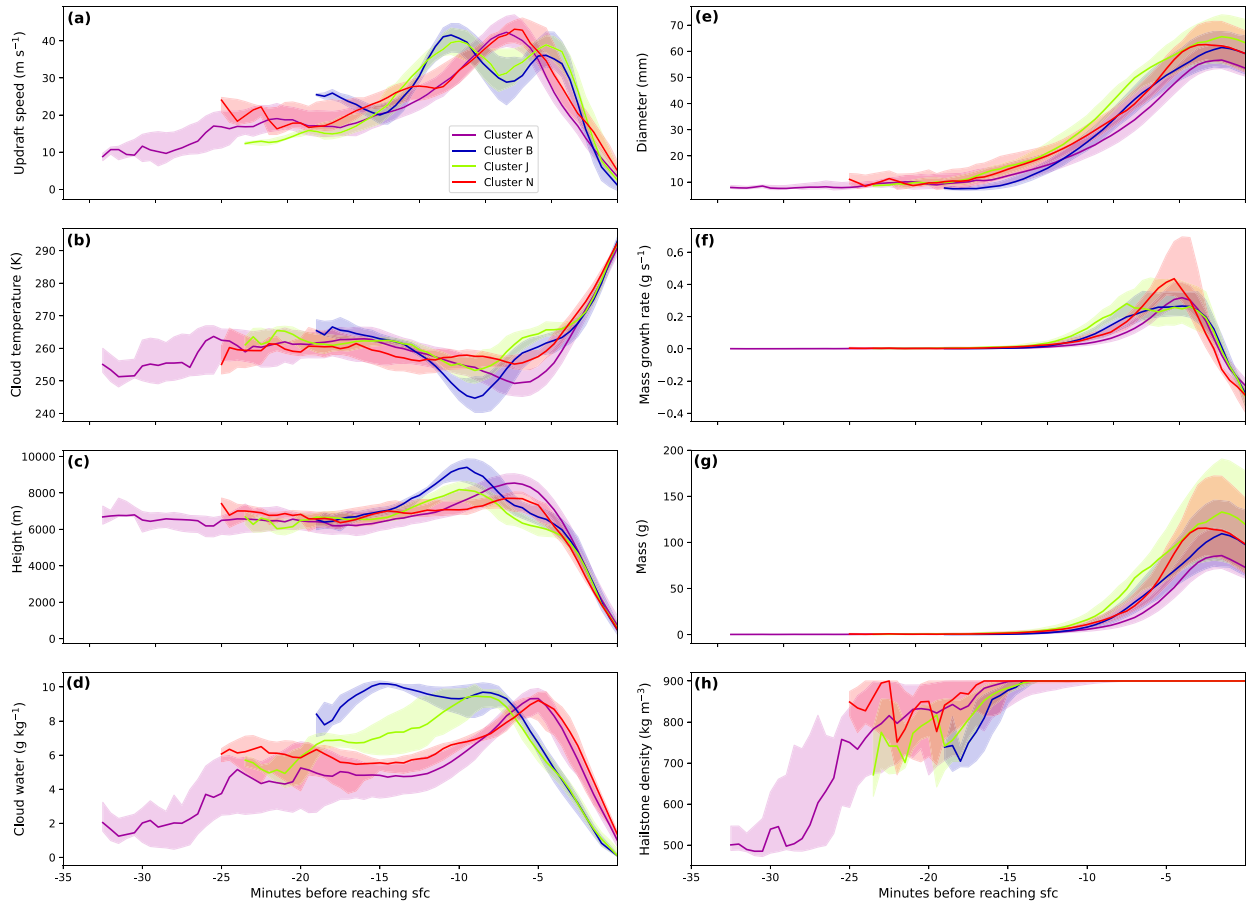
FIG. 18. Line plots of clusters A (purple), B (blue), J (green), and N (yellow) describing the 50th percentile (solid line) and 25th–75th percentile (shaded area) environmental characteristics and hailstone characteristics along the trajectory pathway before reaching the surface. Variables included are (a) updraft speed (m s^{-1}), (b) cloud temperature (K), (c) height (km), (d) cloud liquid water (g kg^{-1}), (e) diameter (mm), (f) mass growth rate (g s^{-1}), (g) mass (g), and (h) hailstone density (kg m^{-3}).

c. Supercluster B

Supercluster B begins further south of the updraft than any other supercluster (Fig. 20b). From south of the updraft, supercluster B also follows a counterclockwise path through the mesocyclone, although a small-scale transient loop on the downshear updraft flank implies a pathway (Fig. 20b) broadly similar to the classical Browning and Foote (1976) trajectory model. The residence time of supercluster B in the updraft is
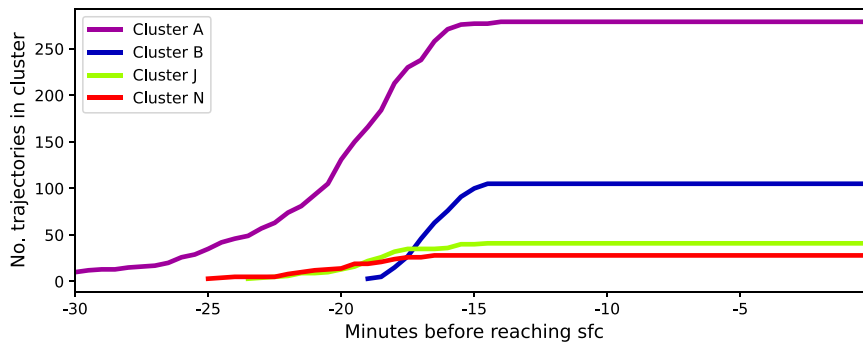
FIG. 19. Number of trajectories included in superclusters A (purple), B (blue), J (green), and N (red) from the start of the first trajectory in cluster until all trajectories reach the surface. The maximum number of trajectories in each supercluster is 279 (A), 105 (B), 41 (J), and 28 (N).
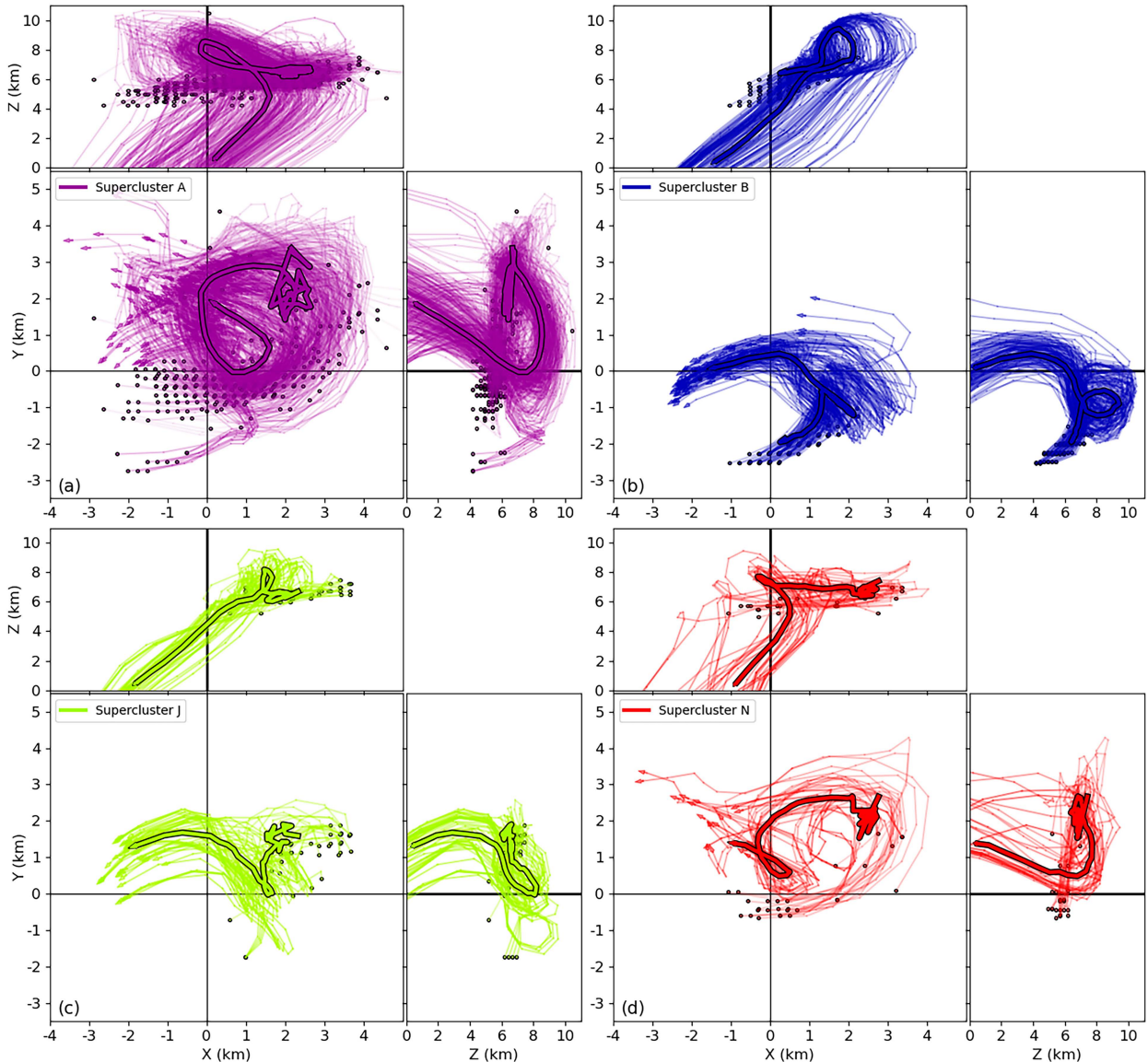
FIG. 20. Individual trajectories from (a) supercluster A, (b) supercluster B, (c) supercluster J, and (d) supercluster N shown in the x–z plane (top), x–y plane (center), and y–z plane (right). Black outlined dots represent the initial trajectory position while arrows represent the final position of the hailstone. The thicker solid line with black outline is the representative trajectory for the entire supercluster. The black lines through (0, 0) denote the updraft center.

the shortest (only ~20 min) of the four superclusters, which is consistent with the large supercooled cloud liquid water along the trajectory (Fig. 18d) that promotes efficient and steady mass growth (Fig. 18e). Additionally, supercluster B achieves solid-ice density shortly after its trajectories begin, leading to a longer period of efficient growth. Superclusters C and M (not shown) additionally show some similar characteristics to supercluster B, in short residence times and large hailstones.

d. Cluster J

Supercluster J results in the largest average hailstones in diameter (Fig. 18e) and mass (Fig. 18g) despite its shorter residence time (~25 min). Supercluster J experiences a large mass growth rate (Fig. 18f) sooner than other superclusters and experiences a nearly constant mass growth rate between ~10 and 5 min prior to reaching the surface rather than peaking and beginning its descent. The large mass growth rate of supercluster J also coincides with a decrease in cloud temperature (Fig. 18b) and an increase in updraft speed (Fig. 18a).

Supercluster J shares similarities with supercluster B, notably their greatest mass growth rate (not shown) which occurs far to the southeast (downshear) of the main updraft (Fig. 20c), as well as two peaks at ~13 and ~5 min before reaching the surface in updraft speed (Fig. 18a) and height (Fig. 18c). This is

likely due to these trajectories interacting with each of the dual updraft maxima in the supercell. The dual updraft maxima feature is commonly seen in studies of large hail-producing supercells (Nelson 1983; M88; Tessendorf et al. 2005).

6. Discussion

A common theme throughout the results is the importance of the updraft, whether it be the size, shape, strength, or structure. Horizontal airflow strength and patterns, an important factor in large hail formation, can depend on these variations of the updraft. These aspects of storm structure and the updraft can impact the DDZ, which we hypothesize plays an important role in hail formation generally and particularly in large hail growth.

The idea of the DDZ is not entirely new but has not been defined in the literature. As previously mentioned, other studies have hinted that weak horizontal flow on the updraft edge could increase residence time and produce larger hail (Rasmussen and Heymsfield 1987b; Heymsfield 1983; Foote 1984). More recently, Kumjian et al. (2021) stated that slower horizontal flow in the region through which hailstones are being advected can increase residence time. Slower horizontal flow in the midlevels is our definition of the DDZ and it does increase residence time when hailstones reside within, thus increasing the potential for large hailstones. Grant and van den Heever (2014) noted that higher hail mixing ratios and number concentrations of smaller hailstones were located on the outside northeastern updraft edge due to weaker storm-relative winds in the midlevels (see their Figs. 7, 8, and 10). They attribute this in part to "enhanced collision and coalescence processes due to the larger raindrops present and thus collection efficiencies," which could lead to more efficient hail growth, but specific to low precipitation supercells. They highlight the importance of the DDZ, specifically the favorable microphysics there, without defining the region of "weak storm-relative winds in the midlevels." It was shown that larger hailstones spent more time within higher values of supercooled cloud liquid water and at higher ambient temperatures than smaller hailstones. While this could be resultant of these conditions being more conducive for growth, the trajectory pathways resultant of the largest trajectories remain below ~8 km for the entirety of their life cycle, which leads to the hypothesis that larger hailstones encounter larger amounts of supercooled cloud liquid water and warmer ambient temperatures due to their trajectory pathway—likely controlled by airflow patterns and updraft characteristics.

The results suggest that the updraft size and shape (specifically the orientation of its major horizontal axis relative to the midlevel shear vector) and its collocation with a deep mesocyclone jointly modulate the maximum hailstone size at the surface. Kumjian et al. (2021) stated that updraft expansion would lead to expansion of the updraft region specific to favorable flow patterns to expand, favoring longer residence times for large hail. Maximum hail size increases with increasing trajectory length and duration within the main updraft, which in theory can be achieved by the midlevel shear vector being oriented perpendicular to the updraft's major horizontal axis. For example, initial embryo growth would be increased if the horizontal storm-relative flow is oriented perpendicular to the updraft's major axis due to lengthening the trajectory of the horizontal airflow around the midlevel updraft. In describing the importance of updraft characteristics (specifically broadness), Dennis and Kumjian (2017) stated, "It is not the magnitudes of the process rates or the updraft speed that seems to be the most important for hail growth in this subset of simulations but, rather, the volume in which optimal growth conditions exist." Midlevel airflow patterns oriented as described could result in a more expansive prime growth region, as well as a larger DDZ, and allow for longer residence times within the DDZ. Ultimately, we hypothesize it is more than just updraft width that is important for hail growth—it is the ratio of the updraft length and width and the orientation of the major axis of the updraft to the midlevel horizontal shear vector.

The structure of the updraft, specifically the location of the rotation of the midlevel mesocyclone, is also an important factor in extending residence time. In the case of an elongated updraft with upshear and downshear cores and a midlevel mesocyclone containing a DDZ collocated with the downshear core (as in the present study), further growth to large hail would be aided by particles orbiting the downshear updraft core while decelerating in the DDZ to increase pathlength and duration of prime growth conditions. Tessendorf et al. (2005) demonstrated greater storm-relative divergence around the midlevel updraft when an additional updraft developed on the right flank (downshear), like the Kingfisher supercell, and consequently, hail volumes peaked shortly after exhibiting the stronger downshear updraft structure described herein. In the alternative case of a weak mesocyclone associated with the downshear updraft, particle growth would hypothetically be inhibited by more rapid hail detrainment from the downshear updraft flank. The structure of the updraft and location of maxima are likely important for large hail growth and should be explored further. An important question to be addressed is if in supercells with two updraft maxima, is severe hail production more likely than in a unicellular, quasi-steady updraft?

The combined modulating influence of updraft area and rotation on hail growth could be a key finding in what large hailstone trajectories look like. Similarities in the growth process can be seen in superclusters A and N, the upshear and downshear group, and past literature. These trajectory groupings mentioned resemble that of the "full circuit" trajectory highlighted in Kumjian et al. (2021), where the trajectories are advected around the mesocyclone (albeit it does not have to be around the entirety of the mesocyclone) and then enter an area of increased updraft before falling out of the storm. M88 also found that the largest hailstones resulted from trajectories being advected cyclonically around the mesocyclone. Tessendorf et al. (2005) state that "a region of cyclonically curved flow around the right flank of [the main] updraft was apparently critical for the production of any hail larger than 20 mm," as one of the four conditions they state must be met for large hail production. M88 pointed out that specifically this trajectory pathway had slower horizontal wind speeds than others allowing for the quasi-balance between vertical velocities and terminal velocities to be achieved. Supercluster A and the upshear group, while similar in trajectory pathway for the latter half of the trajectory,

do not start within the prime growth region. This indicates that despite origin, if an embryo can find its way to the updraft region, it can result in a large hailstone in the same way an embryo sourced close to the updraft.

A variety of trajectory clusters are seen throughout the storm's life cycle, with the largest variations in surface hailstones seen reaching the ground between 2341–2351 UTC and 0001–0016 UTC (not shown). However, there were also clusters that contained trajectories that reached the surface both early and late in the analysis period, meaning that even if the storm evolved (strengthened), a similar trajectory pathway for large hail exists within the storm. This indicates the structure of the storm itself is important to the shape of trajectory pathways, as there are no drastic environmental changes from the start to the end of the analysis period (although it cannot be concluded that subtle environmental changes are not the cause). The minor variations in trajectory pathways could likely be due to differences in horizontal airflow strength and patterns. Although multiple clustered trajectory pathways exhibit notable variations in spatial structure, physical hailstone characteristics, and ambient environment properties following the motion, all superclusters result in hailstones at the surface exceeding 4.5 cm in diameter. The clustered trajectory analysis thus broadly supports the hypothesis that the large hail growth process (although complex and highly nonlinear) appears to possess a "self-organizing" characteristic [e.g., analogous to ideas proposed by Parker (2021)] similar to the existence of attractors in an otherwise somewhat chaotic process.

7. Conclusions

This study has described the ASZ16-HAILCAST hail growth trajectory model and applied it via assimilated input radar and diabatic Lagrangian analyses to yield a novel hail trajectory dataset containing over 2.7 million individual trajectories spanning a range of final hail sizes. This dataset is used to advance process understanding of possible supercell hailstone growth trajectories with respect to their in-storm growth environment, hailstone growth, and decay mechanisms, and evolving hailstone physical characteristics following the particle motion.

In the case presented, it is found that hailstones are more likely to reside near the downshear, mesocyclonic updraft maximum during their growth phase than in the upshear, nonmesocyclonic updraft maximum. Horizontal airflow moves through the midtropospheric mesocyclone, curves counterclockwise around the updraft core, and decelerates through the DDZ to generate elevated horizontal convergence. Hailstones are advected within the cyclonic horizontal airflow pattern around the updraft, although their continued cyclonic advection becomes limited once the DDZ is reached due to horizontal convergence resulting in minimal storm-relative flow. The present findings thus imply that gauging large hail growth potential should likely take into account not only kinematic metrics such as updraft width and shape but also the topology of the horizontal airflow patterns which in turn modulates the resulting hail trajectory distribution. Thus, consideration should be given to the complex nonlinear balance between hail growth and evolving 3D airflow, in which updraft shape, orientation, and placement relative to the midlevel

shear vector are important for generating a favorable internal horizontal airflow pattern aloft associated with increased hail residence time. Overall, we found that horizontal airflow patterns are important to maintaining a quasi-balance between velocities, thus increasing hailstone residence time and likely overall size at the surface. Other studies have also come to this conclusion (English 1973; Nelson 1983; Foote 1984; Tessendorf et al. 2005). Specifically, we conclude that midlevel horizontal flow patterns have the following impacts on hail growth:

- The highest concentrations of melted particles aloft are found where midlevel horizontal winds are strongest, specifically on the northeast of the left flank of the midlevel updraft.
- The highest trajectory concentrations that result in nonmelted surface hailstones spend a majority of their life cycle within regions of the storm where midlevel horizontal winds are weakest during their growth stage.
- The largest concentrations of severe hailstones aloft reside closer to the updraft within the mesocyclone, ultimately being advected into the downshear deceleration zone (DDZ) where the local cloud environment is shielded from shear and entrainment depletion of supercooled cloud liquid water.
- Storm-relative shear at midlevels (midlevel shear vector) being oriented perpendicular to the major (long) axis of the updraft would likely enlarge the DDZ, thus possibly extending the time hailstones spend in the DDZ and expanding the number of hailstones present in the DDZ.

The present comprehensive analysis of the dominant ensembled hail trajectories as functions of internal storm airflow and microphysical growth environments supports the following conclusions about hail growth:

- The largest hailstones, while associated with a variety of trajectory structures, did all generally pass through the DDZ, where horizontal winds minimally impact the hailstones, and they gradually move toward higher vertical velocities while remaining within favorable growth conditions until the updraft can no longer support their terminal velocities. These hailstones tend to fall to ground closest to the updraft core.
- As the supercell structure evolves and a back-sheared anvil develops, it likely serves as a contributing source region for hailstone embryos. Despite initially unfavorable conditions (i.e., in weak vertical velocities outside supercooled cloud), surface severe hail results from trajectories originating in the back-sheared anvil source region.

While airflow patterns are likely the most important feature on the growth of large hailstones, certain conditions must also be present in the storm regarding updraft vertical velocities, supercooled cloud liquid water availability, and ambient temperatures. Previous works have defined a range of values that are supportive of hail growth. In an analysis of time spent during growth within a range of values of these variables for varying hailstone sizes, we found the following:

- Vertical velocities ≥ 40 m s^{-1} are supportive of severe hail growth.

- Hailstones in the vicinity of vertical velocities within <10 m s^{-1} of their terminal velocities are key to the growth of large hail.
- Larger hailstones spend more time growing in higher supercooled cloud liquid water, although a portion of their growth does occur when in lower values of supercooled cloud liquid water.
- The current definition of the HGZ could be shifted from a lower bound at $-10°C$ to include warmer temperatures, as hailstones, specifically larger hailstones, spend a nonnegligible amount of time growing in ambient temperatures between $-10°C$ and the melting level.

Therefore, the prime growth region has been defined as any region of the storm containing vertical velocities greater than 10 m s^{-1} in the deep main updraft core(s), any amount of supercooled cloud liquid water, and ambient temperatures between $0°$ and $-40°C$. Although the lower bounds of these values may not be indicative of where hailstones encounter the highest growth rates, hailstones that become large can begin their growth in low supercooled liquid water and must reside in relatively weak vertical velocities to initially remain aloft in supercooled cloudy updraft prior to transition to stronger updrafts and larger cloud water contents. The all-encompassing definition is needed to include smaller, but still severe hailstones that can result from the lower bound values. Future work should further explore the rate of growth for hailstones of varying sizes under this broader definition of the prime growth region.

In an environmental study of a large sample of hailstorms, Nixon et al. (2023) emphasized that the storm itself could "heavily influence" final hail size, further encouraging future studies of large hail to focus on storm structure. While only one case is presented here, we believe these concluding hypotheses can guide further research on what storm-scale features are important for hail growth and encourage future work to explore these features with larger datasets. With improved knowledge of hail trajectory paths and their relationship to evolving in-storm kinematic, thermal, and microphysical characteristics, the surface impacts of severe and large hail can be further explored. Further exploration of the updraft's distribution of vertical velocity maxima, including the present mode of a supercell updraft containing two maxima, presents a promising avenue of future research to help improve understanding of how growing hailstones interact with complex and somewhat nonsteady updraft evolution. A demonstration that trajectories that interact with the DDZ modality consistently produce the largest hail in additional storm analyses would in turn suggest that observing or predicting the DDZ could help improve hail growth process understanding and facilitate nowcasts of hailstone size limits in specific storms. In a follow-on study, characteristics of all hailstones from the 2.7 million simulated trajectories that reached the surface can be explored, including size-sorting effects within the storm due to horizontal wind shears. The ASZ16-HAILCAST model hail growth physics has additionally been modified to simulate oblate spheroidal hailstones (e.g., English 1973), thus potentially better resolving larger, more physically realistic maximum hailstone dimensions with

verification against detailed surface in situ hail samples (e.g., Pounds 2022; Z83).

Data availability statement. Radiosonde data and the University of Oklahoma School of Meteorology (dual SRs) data are available online from the DC3 EOL data catalog via the URL http://catalog.eol.ucar.edu/dc3/. The 3D hail trajectory software applying ASZ-HAILCAST in simulated storms is available through the public GitHub repository: http://github.com/adams-selin/cm1-4dhailcast with additional information available at http://hailcast.aer.com/. The complementing hail trajectory software for radar-analyzed storm airflow and retrieved thermal-microphysical fields (as applied in the present study) is available on request from the second author. The trajectory clustering package is available via the GitHub repository at http://github.com/adams-selin/trajectory_clustering.

REFERENCES

Adams-Selin, R. D., 2023: A three-dimensional hail trajectory clustering technique. *Mon. Wea. Rev.*, **151**, 2361–2375, https://doi.org/10.1175/MWR-D-22-0345.1.

——, and C. L. Ziegler, 2016: Forecasting hail using a one-dimensional hail growth model within WRF. *Mon. Wea. Rev.*, **144**, 4919–4939, https://doi.org/10.1175/MWR-D-16-0027.1.

——, A. J. Clark, C. J. Melick, S. R. Dembek, I. L. Jirak, and C. L. Ziegler, 2019: Evolution of WRF-HAILCAST during the 2014–16 NOAA/Hazardous Weather Testbed Spring Forecasting Experiments. *Wea. Forecasting*, **34**, 61–79, https://doi.org/10.1175/WAF-D-18-0024.1.

——, and Coauthors, 2023: Just what is "good"? Musings on hail forecast verification through evaluation of FV3-HAILCAST hail forecasts. *Wea. Forecasting*, **38**, 371–387, https://doi.org/10.1175/WAF-D-22-0087.1.

Barth, M. C., and Coauthors, 2015: The Deep Convective Clouds and Chemistry (DC3) field campaign. *Bull. Amer. Meteor. Soc.*, **96**, 1281–1309, https://doi.org/10.1175/BAMS-D-13-00290.1.

Bela, M. M., and Coauthors, 2018: Effects of scavenging, entrainment, and aqueous chemistry on peroxides and formaldehyde in deep convective outflow over the central and southeast United States. *J. Geophys. Res. Atmos.*, **123**, 7594–7614, https://doi.org/10.1029/2018JD028271.

Bolton, D., 1980: The computation of equivalent potential temperature. *Mon. Wea. Rev.*, **108**, 1046–1053, https://doi.org/10.1175/1520-0493(1980)108<1046:TCOEPT>2.0.CO;2.

Brimelow, J. C., G. W. Reuter, and E. R. Poolman, 2002: Modeling maximum hail size in Alberta thunderstorms. *Wea. Forecasting*, **17**, 1048–1062, https://doi.org/10.1175/1520-0434(2002)017<1048:MMHSIA>2.0.CO;2.

——, ——, R. Goodson, and T. W. Krauss, 2006: Spatial forecasts of maximum hail size using prognostic model soundings and HAILCAST. *Wea. Forecasting*, **21**, 206–219, https://doi.org/10.1175/WAF915.1.

Browning, K. A., 1963: The growth of large hail within a steady updraught. *Quart. J. Roy. Meteor. Soc.*, **89**, 490–506, https://doi.org/10.1002/qj.49708938206.

——, and G. B. Foote, 1976: Air-flow and hail growth in supercell storms and some implications for hail suppression. *Quart. J. Roy. Meteor. Soc.*, **102**, 499–533, https://doi.org/10.1002/qj.49710243303.

Chmielewski, V. C., D. R. MacGorman, C. L. Ziegler, E. DiGangi, D. Betten, and M. Biggerstaff, 2020: Microphysical and transportive contributions to normal and anomalous polarity subregions in the 29–30 May 2012 Kingfisher storm. *J. Geophys. Res. Atmos.*, **125**, e2020JD032384, https://doi.org/10.1029/2020JD032384.

Conway, J. W., and D. S. Zrnić, 1993: A study of embryo production and hail growth using dual-Doppler and multiparameter radars. *Mon. Wea. Rev.*, **121**, 2511–2528, https://doi.org/10.1175/1520-0493(1993)121<2511:ASOEPA>2.0.CO;2.

Davenport, C. E., C. L. Ziegler, and M. I. Biggerstaff, 2019: Creating a more realistic idealized supercell thunderstorm evolution via incorporation of base-state environmental variability. *Mon. Wea. Rev.*, **147**, 4177–4198, https://doi.org/10.1175/MWR-D-18-0447.1.

Davies-Jones, R. P., 1974: Discussion of measurements inside high-speed thunderstorm updrafts. *J. Appl. Meteor.*, **13**, 710–717, https://doi.org/10.1175/1520-0450(1974)013<0710:DOMIHS>2.0.CO;2.

Dennis, E. J., and M. R. Kumjian, 2017: The impact of vertical wind shear on hail growth in simulated supercells. *J. Atmos. Sci.*, **74**, 641–663, https://doi.org/10.1175/JAS-D-16-0066.1.

DiGangi, E. A., D. R. MacGorman, C. L. Ziegler, D. Betten, M. Biggerstaff, M. Bowlan, and C. K. Potvin, 2016: An overview of the 29 May 2012 Kingfisher supercell during DC3. *J. Geophys. Res. Atmos.*, **121**, 14316–14343, https://doi.org/10.1002/2016JD025690.

——, C. L. Ziegler, and D. R. MacGorman, 2021: Lightning and secondary convection in the anvil of the May 29, 2012 Oklahoma supercell storm observed by DC3. *J. Geophys. Res. Atmos.*, **126**, e2020JD033114, https://doi.org/10.1029/2020JD033114.

English, M., 1973: Growth of large hail in the storm. *Alberta Hailstorms*, *Meteor. Monogr.*, No. 36, Amer. Meteor. Soc., 37–98, https://doi.org/10.1007/978-1-935704-32-4_2.

Ester, M., H.-P. Kriegel, J. Sander, and X. Xu, 1996: A density-based algorithm for discovering clusters in large spatial databases with noise. *KDD'96 Proc. Second Int. Conf. on Knowledge Discovery and Data Mining*, Portland, OR, Association for the Advancement of Artificial Intelligence, 226–231, https://dl.acm.org/doi/10.5555/3001460.3001507.

Foote, G. B., 1984: A study of hail growth utilizing observed storm conditions. *J. Climate Appl. Meteor.*, **23**, 84–101, https://doi.org/10.1175/1520-0450(1984)023<0084:ASOHGU>2.0.CO;2.

Goyer, G. G., S. S. Lin, S. N. Gitlin, and M. N. Plooster, 1969: On the heat transfer to ice spheres and the freezing of spongy hail. *J. Atmos. Sci.*, **26**, 319–326, https://doi.org/10.1175/1520-0469(1969)026<0319:OTHTTI>2.0.CO;2.

Grant, L. D., and S. C. van den Heever, 2014: Microphysical and dynamical characteristics of low-precipitation and classic supercells. *J. Atmos. Sci.*, **71**, 2604–2624, https://doi.org/10.1175/JAS-D-13-0261.1.

Heymsfield, A. J., 1978: The characteristics of graupel particles in northeastern Colorado cumulus congestus clouds. *J. Atmos. Sci.*, **35**, 284–295, https://doi.org/10.1175/1520-0469(1978)035<0284:TCOGPI>2.0.CO;2.

——, 1982: A comparative study of the rates of development of potential graupel and hail embryos in High Plains storms. *J. Atmos. Sci.*, **39**, 2867–2897, https://doi.org/10.1175/1520-0469(1982)039<2867:ACSOTR>2.0.CO;2.

——, 1983: Case study of a hailstorm in Colorado. Part IV: Graupel and hail growth mechanisms deduced through particle trajectory calculations. *J. Atmos. Sci.*, **40**, 1482–1509, https://doi.org/10.1175/1520-0469(1983)040<1482:CSOAHI>2.0.CO;2.

——, and D. J. Musil, 1982: Case study of a hailstorm in Colorado. Part II: Particle growth processes at mid-levels deduced form in-situ measurements. *J. Atmos. Sci.*, **39**, 2847–2866, https://doi.org/10.1175/1520-0469(1982)039<2847:CSOAHI>2.0.CO;2.

——, and J. C. Pflaum, 1985: A quantitative assessment of the accuracy of techniques for calculating graupel growth. *J. Atmos. Sci.*, **42**, 2264–2274, https://doi.org/10.1175/1520-0469(1985)042<2264:AQAOTA>2.0.CO;2.

——, A. R. Jameson, and H. W. Frank, 1980: Hail growth mechanisms in a Colorado storm. Part II: Hail formation processes. *J. Atmos. Sci.*, **37**, 1779–1807, doi.org/10.1175/1520-0469(1980)037<1779:HGMIAC>2.0.CO;2.

Homeyer, C. R., E. M. Murillo, and M. R. Kumjian, 2023: Relationships between 10 years of radar-observed supercell characteristics and hail potential. *Mon. Wea. Rev.*, **151**, 2609–2632, https://doi.org/10.1175/MWR-D-23-0019.1.

Hosek, M. J., C. L. Ziegler, M. I. Biggerstaff, T. A. Murphy, and Z. Wang, 2023: Relation between Baroclinity, Horizontal Vorticity, and Mesocyclone Evolution in the 6–7 April 2018 Monroe, Louisiana, tornadic supercell during VORTEX-SE. *Mon. Wea. Rev.*, **151**, 2949–2976, https://doi.org/10.1175/MWR-D-22-0313.1.

Jewell, R., and J. Brimelow, 2009: Evaluation of Alberta hail growth model using severe hail proximity soundings from the United States. *Wea. Forecasting*, **24**, 1592–1609, https://doi.org/10.1175/2009WAF2222230.1.

Johnson, A. W., and K. E. Sugden, 2014: Evaluation of sounding derived thermodynamic and wind-related parameters associated with large hail events. *Electron. J. Severe Storms Meteor.*, **9** (5), https://ejssm.org/archives/2014/vol-9-5-2014/.

Kennedy, P. C., and A. G. Detwiler, 2003: A case study of the origin of hail in a multicell thunderstorm using in situ aircraft and polarimetric radar data. *J. Appl. Meteor.*, **42**, 1679–1690, https://doi.org/10.1175/1520-0450(2003)042<1679:ACSOTO>2.0.CO;2.

Knight, C. A., and N. C. Knight, 1970: The falling behavior of hailstones. *J. Atmos. Sci.*, **27**, 672–681, https://doi.org/10.1175/1520-0469(1970)027<0672:TFBOH>2.0.CO;2.

——, and K. R. Knupp, 1986: Precipitation growth trajectories in a CCOPE storm. *J. Atmos. Sci.*, **43**, 1057–1073, https://doi.org/10.1175/1520-0469(1986)043<1057:PGTIAC>2.0.CO;2.

——, and N. C. Knight, 2001: Hailstorms. *Severe Convective Storms, Meteor. Monogr.*, No. 28, Amer. Meteor. Soc., 223–248, https://doi.org/10.1175/0065-9401-28.50.223.

——, and ——, 2005: Very large hailstones from Aurora, Nebraska. *Bull. Amer. Meteor. Soc.*, **86**, 1773–1782, https://doi.org/10.1175/BAMS-86-12-1773.

——, D. H. Ehhalt, N. Roper, and N. C. Knight, 1975: Radial and tangential variation of deuterium in hailstones. *J. Atmos. Sci.*, **32**, 1990–2000, https://doi.org/10.1175/1520-0469(1975)032<1990:RATVOD>2.0.CO;2.

——, N. C. Knight, and K. A. Kime, 1981: Deuterium contents of storm inflow and hailstone growth layers. *J. Atmos. Sci.*, **38**, 2485–2499, https://doi.org/10.1175/1520-0469(1981)038<2485:DCOSIA>2.0.CO;2.

——, P. T. Schlatter, and T. W. Schlatter, 2008: An unusual hailstorm on 24 June 2006 in Boulder, Colorado. Part II: Low-density growth of hail. *Mon. Wea. Rev.*, **136**, 2833–2348, https://doi.org/10.1175/2008MWR2338.1.

Kumjian, M. R., and K. Lombardo, 2020: A hail growth trajectory model for exploring the environmental controls on hail size: Model physics and idealized tests. *J. Atmos. Sci.*, **77**, 2765–2791, https://doi.org/10.1175/JAS-D-20-0016.1.

——, K. A. Lombardo, and S. Loeffler, 2021: The evolution of hail production in simulated supercell storms. *J. Atmos. Sci.*, **78**, 3417–3440, https://doi.org/10.1175/JAS-D-21-0034.1.

Lee, J.-G., J. Han, and K.-Y. Whang, 2007: Trajectory clustering: A partition-and-group framework. *SIGMOD'07: Proc. 2007 ACM SIGMOD Int. Conf. on Management of Data*, Beijing, China, Association for Computing Machinery, 593–604, https://dl.acm.org/doi/10.1145/1247480.1247546.

Lesins, G. B., and R. List, 1986: Sponginess and drop shedding of gyrating hailstones in a pressure-controlled icing wind tunnel. *J. Atmos. Sci.*, **43**, 2813–2825, https://doi.org/10.1175/1520-0469(1986)043<2813:SADSOG>2.0.CO;2.

Lin, Y., and M. R. Kumjian, 2022: Influences of CAPE on hail production in simulated supercell storms. *J. Atmos. Sci.*, **79**, 179–204, https://doi.org/10.1175/JAS-D-21-0054.1.

Mansell, E. R., C. L. Ziegler, and E. C. Bruning, 2010: Simulated electrification of a small thunderstorm with two-moment bulk microphysics. *J. Atmos. Sci.*, **67**, 171–194, https://doi.org/10.1175/2009JAS2965.1.

Miller, L. J., and J. C. Fankhauser, 1983: Radar echo structure, air motion and hail formation in a large stationary multicellular thunderstorm. *J. Atmos. Sci.*, **40**, 2399–2418, https://doi.org/10.1175/1520-0469(1983)040<2399:RESAMA>2.0.CO;2.

——, J. D. Tuttle, and C. A. Knight, 1988: Airflow and hail growth in a severe northern plains supercell. *J. Atmos. Sci.*, **45**, 736–762, https://doi.org/10.1175/1520-0469(1988)045<0736:AAHGIA>2.0.CO;2.

——, ——, and G. B. Foote, 1990: Precipitation production in a large Montana hailstorm: Airflow and particle growth trajectories. *J. Atmos. Sci.*, **47**, 1619–1646, https://doi.org/10.1175/1520-0469(1990)047<1619:PPIALM>2.0.CO;2.

Morgan, G. M., Jr., 1972: On the growth of large hail. *Mon. Wea. Rev.*, **100**, 196–205, https://doi.org/10.1175/1520-0493(1972)100<0196:OTGOLH>2.3.CO;2.

Musil, D. J., 1970: Computer modeling of hailstone growth in feeder clouds. *J. Atmos. Sci.*, **27**, 474–482, https://doi.org/10.1175/1520-0469(1970)027<0474:CMOHGI>2.0.CO;2.

——, A. J. Heymsfield, and P. L. Smith, 1986: Microphysical characteristics of a well-developed weak echo region in a High-Plains supercell thunderstorm. *J. Climate Appl. Meteor.*, **25**, 1037–1051, https://doi.org/10.1175/1520-0450(1986)025<1037:MCOAWD>2.0.CO;2.

Nelson, S. P., 1983: The influence of storm flow structure on hail growth. *J. Atmos. Sci.*, **40**, 1965–1983, https://doi.org/10.1175/1520-0469(1983)040<1965:TIOSFS>2.0.CO;2.

——, 1987: The hybrid multicellular–supercellular storm—An efficient hail producer. Part II: General characteristics and implications for hail growth. *J. Atmos. Sci.*, **44**, 2060–2073, https://doi.org/10.1175/1520-0469(1987)044<2060:THMSEH>2.0.CO;2.

——, and N. C. Knight, 1987: The hybrid multicellular–supercellular storm—An efficient hail producer. Part I: An archetypal example. *J. Atmos. Sci.*, **44**, 2042–2059, doi.org/10.1175/1520-0469(1987)044%3c2042:THMSEH>2.0.CO;2.

Nixon, C. J., and J. T. Allen, 2022: Distinguishing between hodographs of severe hail and tornadoes. *Wea. Forecasting*, **37**, 1761–1782, https://doi.org/10.1175/WAF-D-21-0136.1.

——, ——, and M. Taszarek, 2023: Hodographs and skew *T*s of hail-producing storms. *Wea. Forecasting*, **38**, 2217–2236, https://doi.org/10.1175/WAF-D-23-0031.1.

Paluch, I. R., 1978: Size sorting of hail in a three-dimensional updraft and implications for hail suppression. *J. Appl. Meteor.*, **17**, 763–777, https://doi.org/10.1175/1520-0450(1978)017<0763:SSOHIA>2.0.CO;2.

Parker, M. D., 2021: Self-organization and maintenance of simulated nocturnal convective systems from PECAN. *Mon. Wea. Rev.*, **149**, 999–1022, https://doi.org/10.1175/MWR-D-20-0263.1.

Peters, J. M., C. J. Nowotarski, and H. Morrison, 2019: The role of vertical wind shear in modulating maximum supercell updraft velocities. *J. Atmos. Sci.*, **76**, 3169–3189, https://doi.org/10.1175/JAS-D-19-0096.1.

——, H. Morrison, C. J. Nowotarski, J. P. Mulholland, and R. L. Thompson, 2020: A formula for the maximum vertical velocity in supercell updrafts. *J. Atmos. Sci.*, **77**, 3747–3757, https://doi.org/10.1175/JAS-D-20-0103.1.

Picca, J., and A. Ryzhkov, 2012: A dual-wavelength polarimetric analysis of the 16 May 2010 Oklahoma City extreme hailstorm. *Mon. Wea. Rev.*, **140**, 1385–1403, https://doi.org/10.1175/MWR-D-11-00112.1.

Poolman, E. R., 1992: Die voorspelling van haelkorrelgroei in Suid-Afrika (The forecasting of hail growth in South Africa). M.S. thesis, Dept. of Engineering, University of Pretoria, 113 pp.

Potvin, C. K., L. J. Wicker, and A. Shapiro, 2012a: Assessing errors in variational dual-Doppler wind syntheses of supercell thunderstorms observed by storm-scale mobile radars. *J. Atmos. Oceanic Technol.*, **29**, 1009–1025, https://doi.org/10.1175/JTECH-D-11-00177.1.

——, D. Betten, L. J. Wicker, K. L. Elmore, and M. I. Biggerstaff, 2012b: 3DVAR versus traditional dual-Doppler wind retrievals of a simulated supercell thunderstorm. *Mon. Wea. Rev.*, **140**, 3487–3494, https://doi.org/10.1175/MWR-D-12-00663.1.

Pounds, L. E., 2022: Hailstone trajectory and surface hailfall analysis in the 29-30 May 2012 Kingfisher, OK supercell. M.S. thesis, School of Meteorology, The University of Oklahoma, 154 pp., https://hdl.handle.net/11244/335544.

Pruppacher, H. R., and J. D. Klett, 1997: *Microphysics of Clouds and Precipitation*. 2nd ed. Kluwer Academic, 954 pp.

Rasmussen, R. M., and A. J. Heymsfield, 1985: A generalized form for impact velocities used to determine graupel accretional densities. *J. Atmos. Sci.*, **42**, 2275–2279, https://doi.org/10.1175/1520-0469(1985)042<2275:AGFFIV>2.0.CO;2.

——, and ——, 1987a: Melting and shedding of graupel and hail. Part I: Model physics. *J. Atmos. Sci.*, **44**, 2754–2763, https://doi.org/10.1175/1520-0469(1987)044<2754:MASOGA>2.0.CO;2.

——, and ——, 1987b: Melting and shedding of graupel and hail. Part III: Investigation of the role of shed drops as hail embryos in the 1 August CCOPE severe storm. *J. Atmos. Sci.*, **44**, 2783–2803, https://doi.org/10.1175/1520-0469(1987)044<2783:MASOGA>2.0.CO;2.

Schubert, E., J. Sander, M. Ester, H. P. Kriegel, and X. Xu, 2017: DBSCAN revisited, revisited: Why and how you should (still) use DBSCAN. *ACM Trans. Database Syst.*, **42**, 1–21, https://doi.org/10.1145/3068335.

Taszarek, M., H. E. Brooks, and B. Czernecki, 2017: Sounding derived parameters associated with convective hazards in Europe. *Mon. Wea. Rev.*, **145**, 1511–1528, https://doi.org/10.1175/MWR-D-16-0384.1.

Tessendorf, S. A., L. J. Miller, K. C. Wiens, and S. A. Rutledge, 2005: The 29 June supercell observed during STEPS. Part I: Kinematics and microphysics. *J. Atmos. Sci.*, **62**, 4127–4150, https://doi.org/10.1175/JAS3585.1.

Wade, A., M. C. Coniglio, and C. L. Ziegler, 2018: Comparison of near- and far-field supercell inflow environments using radiosonde observations. *Mon. Wea. Rev.*, **146**, 2403–2415, https://doi.org/10.1175/MWR-D-17-0276.1.

Waugh, S. M., C. L. Ziegler, and D. R. MacGorman, 2018: In situ microphysical observations of the 29–30 May 2012 Kingfisher, OK, supercell with a balloon-borne video disdrometer. *J. Geophys. Res. Atmos.*, **123**, 5618–5640, https://doi.org/10.1029/2017JD027623.

Yang, Q., and Coauthors, 2015: Aerosol transport and wet scavenging in deep convective clouds: A case study and model evaluation using a multiple passive tracer analysis approach. *J. Geophys. Res. Atmos.*, **120**, 8448–8468, https://doi.org/10.1002/2015JD023647.

Ziegler, C. L., 1985: Retrieval of thermal and microphysical variables in observed convective storms. Part I: Model development and preliminary testing. *J. Atmos. Sci.*, **42**, 1487–1509, https://doi.org/10.1175/1520-0469(1985)042<1487:ROTAMV>2.0.CO;2.

——, 1988: Retrieval of thermal and microphysical variables in observed convective storms. Part II: Sensitivity of cloud processes to variation of the microphysical parameterization. *J. Atmos. Sci.*, **45**, 1072–1090, https://doi.org/10.1175/1520-0469(1988)045<1072:ROTAMV>2.0.CO;2.

——, 2013a: A diabatic Lagrangian technique for the analysis of convective storms. Part I: Description and validation via an observing system simulation experiment. *J. Atmos. Oceanic Technol.*, **30**, 2248–2265, https://doi.org/10.1175/JTECH-D-12-00194.1.

——, 2013b: A diabatic Lagrangian technique for the analysis of convective storms. Part II: Application to a radar-observed storm. *J. Atmos. Oceanic Technol.*, **30**, 2266–2280, https://doi.org/10.1175/JTECH-D-13-00036.1.

——, P. S. Ray, and N. C. Knight, 1983: Hail growth in an Oklahoma multicell storm. *J. Atmos. Sci.*, **40**, 1768–1791, https://doi.org/10.1175/1520-0469(1983)040<1768:HGIAOM>2.0.CO;2.

——, D. R. MacGorman, J. E. Dye, and P. S. Ray, 1991: A model evaluation of non-inductive graupel-ice charging in the early electrification of a mountain thunderstorm. *J. Geophys. Res.*, **96**, 12 833–12 855, https://doi.org/10.1029/91JD01246.

——, E. R. Mansell, J. M. Straka, D. R. MacGorman, and D. W. Burgess, 2010: The impact of spatial variations of low-level stability on the life cycle of a simulated supercell storm. *Mon. Wea. Rev.*, **138**, 1738–1766, https://doi.org/10.1175/2009MWR3010.1.